New Projections of Changing Heavy Precipitation in King County

Prepared by the

May 2018 | Climate Impacts Group | University of Washington

Guillaume Mauger, *UW Climate Impacts Group*
Jason Won, *UW Climate Impacts Group*
Katherine Hegewisch, *U. Idaho Department of Geography*
Cary Lynch, *Connecticut Department of Energy & Env. Protection*
Raquel Lorente Plazas, *Univ. of Murcia, Spain*
Yolande Serra, *UW JISAO*
Eric P. Salathé Jr., *UW Bothell*

Cover image: Created at https://wordart.com/create using text from this report.

Acknowledgements

The authors would like to thank Rick Steed for his help in producing the GFDL WRF simulation used in this report, as well as Cliff Mass for his generous donation of computing resources. Robert Norheim produced the interactive online visualizations using Tableau. This project was funded by the King County Department of Natural Resources and Parks and the Washington State Department of Ecology. Additional support came from the Critical Infrastructure Resilience Institute (CIRI), a U.S. Department of Homeland Security S&T Center of Excellence (award number 2015-ST-061-CIRC01).

Recommended Citation

Mauger, G.S., J.S. Won, K. Hegewisch, C. Lynch, R. Lorente Plazas, E. P. Salathé Jr., 2018. New Projections of Changing Heavy Precipitation in King County. Report prepared for the King County Department of Natural Resources. Climate Impacts Group, University of Washington, Seattle.

Table of Contents

1 Executive Summary

Recent research suggests that future heavy rain events will be more intense in the Pacific Northwest (e.g., Warner et al. 2015). Past studies have not accounted for this change, either because the methods cannot reliably capture changes in rainfall intensity (e.g., Abatzoglou and Brown 2012), or because previous studies did not evaluate changes in short-duration precipitation (e.g., hourly) that are of relevance to stormwater planning (e.g., Salathé et al. 2010).

The purpose of this project was to develop projections of 21st century changes in precipitation that can be used to inform stormwater and wastewater management in King County. The work was funded by the King County Department of Natural Resources and Parks and the Washington State Department of Ecology. Additional support came from the Critical Infrastructure Resilience Institute (CIRI), a U.S. Department of Homeland Security S&T Center of Excellence.

The specific objectives of the project were to:

1. ***Produce two new Regional Climate Model projections:*** Evaluate global models and develop projections representing a low- and a high-end scenario for 21st century change in precipitation. Archive hourly precipitation and other fields (e.g., evapotranspiration, wind speed and direction), for the entire model domain.

2. ***Synthesize projections to support wastewater conveyance and treatment system impacts assessment:*** Evaluate changes in the intensity, duration, and magnitude of heavy precipitation events in the region. Explore the possibility of developing a statistically-derived pseudo-ensemble of projected changes by relating large-scale global model projections to local-scale exceedance probabilities.

3. ***Synthesize projections to support countywide stormwater design:*** Develop hourly precipitation time series (1970-2099) for hydrologic model input points.

Using the Weather Research and Forecasting (WRF, Skamarock et al. 2005) regional climate model, we produced two new “dynamically downscaled” projections of future climate. A key feature of these projections is that they provide hourly estimates of future weather conditions (temperature, precipitation, humidity, wind, etc.). This is critical, given that many stormwater facilities are designed based on short-duration rainfall intensities. Results from each simulation were evaluated for 83 rain gauge sites that are currently operated by Seattle and King County for stormwater planning.

Our results show the potential for large increases in future rainfall intensity, for example showing a 7 to 54% increase in the 10-year hourly rainfall extreme at Sea-Tac, by the 2080s. However, results differ substantially among seasons and for the two climate projections considered. Although most projections indicate an increase in precipitation intensity, results for the low-end model project a decrease in precipitation intensity for

some statistics and durations (e.g., the 25-, 50-, and 100-year extremes in hourly precipitation at Sea-Tac). Similarly, most of the projected changes for summer suggest a decrease in precipitation intensity, although this may be affected by the model's limited ability to capture convective events such as thunderstorms. All data, documentation, and findings are made available online, including an interactive tool that allows users to easily navigate to the station and results of interest.

There are two ways in which future work could build on these results. First, by producing additional regional climate model projections. Additional simulations could be obtained via a collaboration with UW Professor Cliff Mass, who is currently producing several new regional model projections under a grant from the Amazon Catalyst program. These new projections would help elucidate our results in two ways: by both increasing the sample size, thereby improving the statistics; and by evaluating results for new global models, which may have different model representations for key processes. Second, we believe there are a number of methodological choices that could be investigated further, including (a) an improved treatment of the precipitation statistics and (b) further optimization of the regional climate model to improve the representation of precipitation extremes.

2 Background

Changes in the intensity, duration, and frequency of precipitation may negatively affect stormwater and wastewater facilities, exacerbate landslide and urban flood risk, and lead to other public safety and water quality concerns. Recent research has shown that heavy rain events are projected to become more intense with climate change (e.g., Warner et al. 2015, Trenberth 2011). This has altered the calculus regarding climate change impacts in the Pacific Northwest, since previous research suggested very little change in precipitation for the region. This is in part due to new methods of "downscaling" the large-scale changes projected by global climate models (GCMs) to smaller-scale changes of relevance to impacts assessment. Studies have shown that a physics-based approach ("dynamical downscaling"), is needed to capture changes in precipitation extremes and the associated impacts (Salathé et al. 2014). Previous approaches relied primarily on an empirical approach ("statistical downscaling"), which does not provide reliable estimates of changes in extremes. In dynamical downscaling, a regional climate model is used to simulate local-scale changes in climate, leading to a better representation of changes in the physical processes at these scales. This distinction is particularly important for precipitation, since dynamical downscaling can explicitly represent the interactions of weather systems with the complex terrain of the Pacific Northwest.

One previous study used dynamical downscaling to assess changes in precipitation for the Pacific Northwest. Rosenberg et al. (2010) evaluated precipitation projections from two regional model simulations, based on the previous generation of regional and global climate models. They found changes in precipitation intensity ranging from -5% to +19% for the 2030s, relative to 1970-2000, for durations ranging from 1 hour to 10 days. This report describes a new set of regional model projections that build on the Rosenberg et al. study. Specifically:

1. The new analysis is based on updated global and regional climate models,
2. Global models were selected to bracket the low- and high-end among projections,
3. We have developed an improved approach to bias correction, and
4. The results span a larger set of metrics and locations.

3 Global Climate Model (GCM) Projections

Regional weather and climate patterns can be influenced by conditions in other parts of the globe. As a result, regional climate model (RCM) simulations can only be produced by using the outputs from a global climate model as boundary conditions. Heavy rain events in the Pacific Northwest are typically driven by "Atmospheric River" (AR) events, in which narrow bands of concentrated moisture are carried into the region from lower latitudes. Previous studies have shown that global models are capable of representing the key aspects of Atmospheric Rivers (e.g., Flato et al. 2013), but lack the resolution to capture the local consequences for precipitation given the complex topography of the Pacific Northwest. This means that: (1) regional climate models are needed to estimate local-scale changes in extreme precipitation, and (2) global climate models are appropriate to use as boundary conditions for these regional climate simulations.

GCM Evaluation

Model evaluation will be described in detail in a forthcoming publication (Lynch and Mauger, in prep); this section summarizes the approach and the results of the evaluation.

Data

GCM projections were obtained from the Climate Model Inter-comparison Project, phase 5 (CMIP5; Taylor et al., 2012). As part of the CMIP5 project, international modeling groups coordinate to create a set of consistent future simulations, driven by predetermined greenhouse gas scenarios ("Representative Concentration Pathways", or RCPs, van Vuuren et al. 2011; see below for a more in-depth discussion). Models were chosen based on availability of daily and monthly data for comparison with observations. Appendix A includes a full list of the GCMs that were included in our evaluations.

Each GCM is often run multiple times for each greenhouse gas scenario, each time with slightly different initial conditions. Since the climate system is chaotic, the small changes in initial conditions result in a different sequence of weather and climate variability in each simulation. Since each of these simulations represents one possible sequence of events for the same boundary conditions – in the same way that a lab experiment might be repeated to determine if the results can be replicated – these are referred to as "realizations".

Although many of the CMIP5 GCMs have multiple realizations, in this study we only used one realization for each model. We did this for two reasons: (1) our GCM evaluation metrics are designed to average out natural variability, which would minimize the effect of considering a different realization, and (2) currently, we cannot afford the computational expense of running multiple realizations through the regional climate model. For simplicity, we used the first realization of each model (for CCSM4, the first realization with valid data was realization 6, or "r6" in the CMIP5 archive; all other models had valid data for "r1").

CMIP5 historical simulations begin as early as 1850. Since start dates vary by model and observational data are limited prior to 1950, we evaluated simulations from the last half of the 20th century (1950-1999) only.

As a proxy for observations, we use the NCEP/NCAR (National Center for Environmental Prediction/National Center for Atmospheric Research Reanalysis) reanalysis 1 (NRA40; Kalnay et al. 1996). The data have a resolution of about 1.9-degrees, with daily fields for the years 1948–2012. This dataset was chosen due to its longer time period and the availability of large-scale atmospheric fields for comparison. Previous studies have shown that the NCEP/NCAR reanalysis accurately represents the large-scale drivers, spatial structure, and timing of precipitation over the Pacific Northwest (PNW), despite its coarse resolution and poor representation of topography (Kalnay et al, 1996; Widmann and Bretherton, 2000; Kistler et al, 2001; Kossin, 2015).

Approach

In order to select a subset of GCMs that are most suited to evaluating changes in the PNW, global models were evaluated against a range of performance metrics aimed at identifying models that best capture the dynamics governing large-scale precipitation in the region. Most GCM rankings involve evaluating model performance against the average and spatial/temporal variability in some climate metric. Although this approach may be appropriate for quantities that vary consistently over large spatial scales such as temperature and surface pressure (i.e., both temperature and surface pressure have long autocorrelation length scales), it is unlikely to be the best approach for precipitation, which is poorly resolved by global models, subject to substantial biases, and confined to statistical representations in many cases. However, research has shown that the large-scale dynamics that drive precipitation are well represented by GCMs.

Given the focus of the current study on stormwater, we developed a set of metrics aimed at evaluating GCM ability to accurately simulate the drivers of heavy precipitation events in the Pacific Northwest U.S. For this study, we chose to emphasize seasonal average conditions related to storm characteristics. This both ensures robust statistics and is consistent with our emphasis on long term climate change as opposed to weather variations. Although additional work could further emphasize synoptic-scale conditions related to storms, this was not deemed feasible within the current scope of work.

ID	*Long Name*	*Latitude*	*Longitude*
PNW	Pacific Northwest	41.5-49.5N	124-111W
WNA	Western North America	20-60N	165-100W
NEPAC	Northeast Pacific	20-60N	165-120W
AL	Aleutian Low	45-65N	180-140W
SH	Northern Pacific Subtropical High	25-45N	155-125W
Ocn-PNW	Nearshore Pacific Northwest	38-52N	135-130W

Table 3.1. List of geographic domains used to evaluate metrics.

The new metrics were combined with a complementary selection of metrics developed by Rupp et al. (2013), which emphasize GCM performance related to temperature, long-term trends and variability, and the seasonal cycle. The geographic regions used to define metrics are listed in Table 3.1, while the metrics themselves are listed in Table 3.2. Note that some metrics were evaluated for several geographic regions in order to focus in on specific mechanisms that may lead to different biases in each.

Table 3.2. GCM evaluation metrics used in this study. Metrics derived from Rupp et al. (2013) are noted in the description; these are listed at the bottom of the table.

Metric	***Geog. Extent***	***Description***
SLP spacecorr	NEPAC	Seasonal average sea level pressure. Spatial correlation between simulated and observed.
	AL	
	SH	
SLP spacebias	NEPAC	Seasonal average sea level pressure, averaged over each domain. Difference between simulated and observed.
	AL	
	SH	
SLP SD	NEPAC	Seasonal average sea level pressure; standard deviation of the spatial pattern within each domain. Ratio of simulated to observed.
	AL	
	SH	
UA spacecorr	NEPAC	Seasonal average zonal wind for all levels from 250-100 hPa. Spatial correlation between simulated and observed.
UA spacebias	NEPAC	Seasonal average zonal wind for all levels from 250-100 hPa, averaged over each domain. Difference between simulated and observed.
PRW95 spacebias	Ocn-PNW	Winter (December-February) 95th percentile of daily precipitable water, averaged over the Nearshore Pacific Northwest domain. Difference between simulated and observed.
PRWsd spacebias	Ocn-PNW	Winter (December-February) standard deviation of daily precipitable water, averaged over the Nearshore Pacific Northwest domain. Difference between simulated and observed.
ZG spacecorr	NEPAC	Seasonal 500mb geopotential height correlation of simulated with mean spatial pattern
ZG spacebias	NEPAC	Seasonal 500mb geopotential height observation minus simulated mean spatial average
ZG SD	NEPAC	Seasonal 500mb geopotential height standard deviation of mean spatial pattern, normalized by standard deviation of observed pattern

Metric	*Geog. Extent*	*Description*
tas_bias	PNW	Average surface temperature, 1960-1999. Difference between simulated and observed. *(from Rupp et al, 2013).*
tas_amp	PNW	Average difference between warmest and coldest month, 1960-1999. Difference between simulated and observed. *(from Rupp et al, 2013).*
pr_amp	PNW	Average difference between wettest and driest month, 1960-1999. Difference between simulated and observed. *(from Rupp et al, 2013).*
tas_trend	PNW	Trend in annual average surface temperature, 1901-1999. Difference between simulated and observed. *(from Rupp et al, 2013).*
tas_var1yr	WNA	Variance in annual average surface temperature, 1901-1999. Difference between simulated and observed. *(from Rupp et al, 2013).*
pr_var1yr	WNA	Coefficient of variation in annual total precipitation, 1902-1999. Difference between simulated and observed. *(from Rupp et al, 2013).*
tas_coDJF	WNA	Average winter (Dec-Feb) surface temperature, 1960-1999. Spatial correlation between simulated and observed. *(from Rupp et al, 2013).*
tas_sdDJF	WNA	Average winter (Dec-Feb) surface temperature, 1960-1999; standard deviation of the spatial pattern within each domain. Ratio of simulated to observed. *(from Rupp et al, 2013).*

Results

Metric ranking closely follows the methodology from previous studies (Pierce et al, 2009; Rupp et al. 2013) where we first treated all metrics equally and ranked models based on the total relative error for all metrics (Figure 3.1). Errors are standardized so that model biases for each metric range from 0 to 1. Models are ordered from lowest mean error (left) to highest mean error (right).

We then chose to qualitatively select metrics that we believed to be strongly related to PNW extreme precipitation, and distilled these using principle components. By requiring orthogonality, a principal components analysis (PC analysis, sometimes referred to as an Empirical Orthogonal Function, or EOF analysis) can be used to reduce redundancy and to obtain a core grouping of significant metrics. As in Rupp et al. (2013) the models were treated as the dependent variable, while the biases for each metric were treated as independent variables in the analysis. The result is a reduced set of metrics that synthesize the unique contributions to the biases across models. North's rule of thumb was used to determine the number of significant principal components (North et al. 1982). The observational dataset was included in the PC analysis, and the euclidean distance from the PC values for observations to those for each model were used to construct an

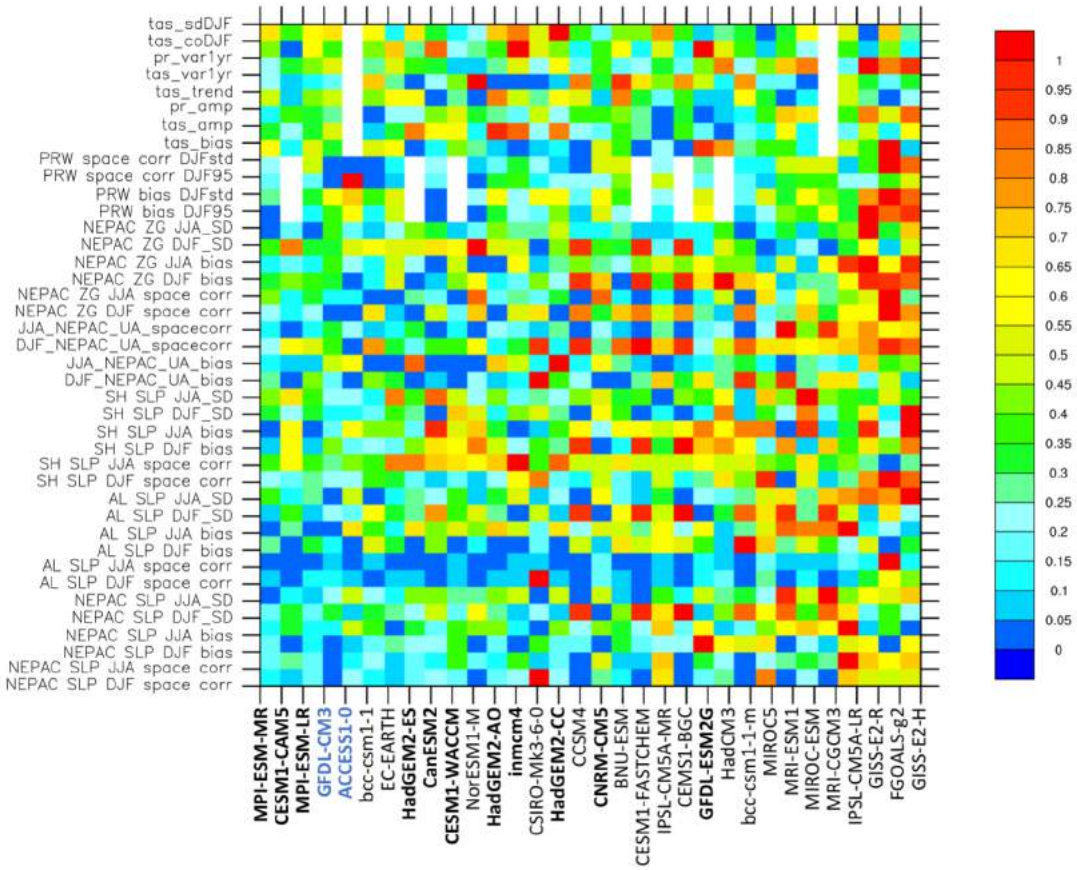

Figure 3.1. As in Rupp et al. (2013, see their Figure 2 for comparison), except showing the results for the new precipitation metrics (Table 3.2) used as a substitute for direct evaluation of GCM precipitation. Relative error of each metric for each GCM. Models are ordered from least (left) to most (right) mean relative error, where mean relative error is the mean of relative errors from all metrics. Top-performing models, based on the current analysis (Table 3.3), are highlighted in bold, and the two selected for RCM downscaling are in blue (GFDL CM3, ACCESS 1.0). White blocks indicate metrics that were not calculated for a particular model due to a lack of available data.

overall error score and then normalized to range from 0 to 1, from least to greatest error (Figure 3.2).

Figure 3.2 includes the rankings for the first three PCs, based on North's rule of thumb, and models are ordered from least (left) to greatest (right) error based on these rankings. For reference, the combined error score for the first two, five, and all PCs are also included in the graph. These comparisons show two things: (1) the rankings all show a fairly consistent overall pattern of model performance, and (2) different combinations of PCs would alter the ranking, though in general the best-performing 10-15 models remain the same. Since the purpose of the current analysis is to remove the worst-performing models, this level of agreement is sufficient to proceed to the task of selecting the two models that will be used to drive the Regional Climate Model (RCM) simulations.

Previous research has shown that model ranking can differ substantially depending on the criteria used for GCM evaluation (e.g., Brekke et al. 2008). Our results confirm this finding: although many of our metrics overlap with those of Rupp et al. (2013), our new

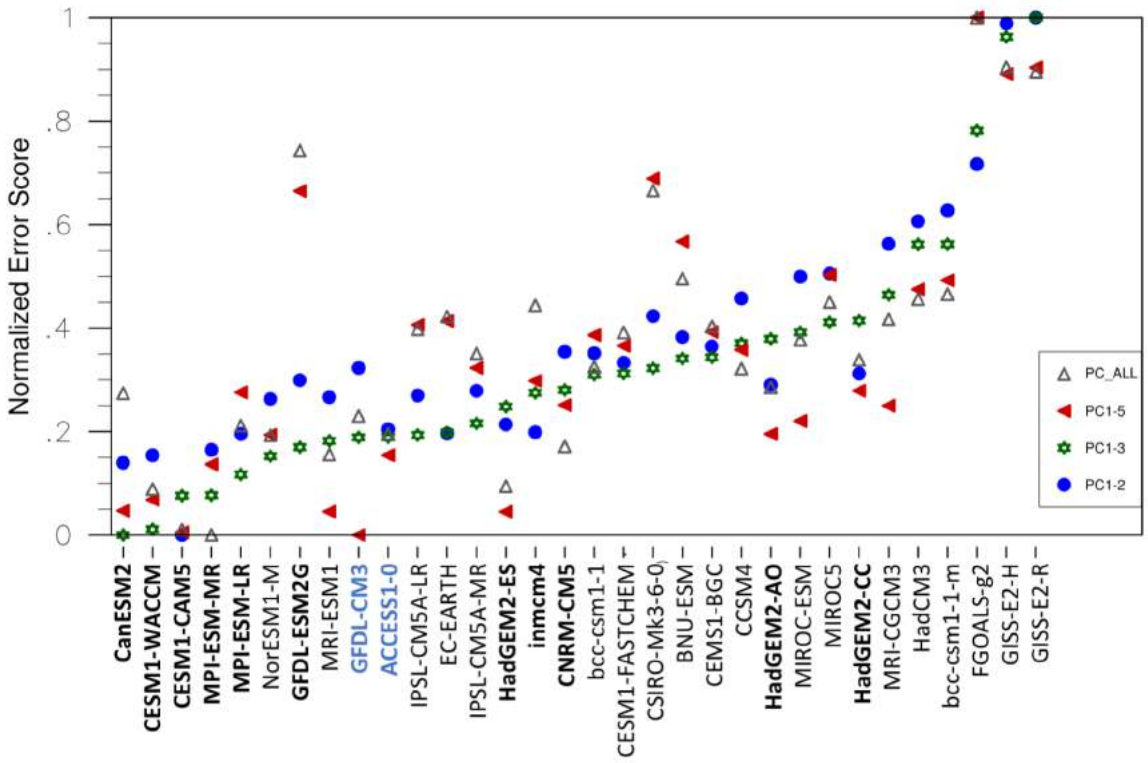

Figure 3.2. As in Rupp et al. (2013, see their Figure 3 for comparison). EOF ranking of models according to normalized error score from principal components analysis of 17 performance metrics. Ranking is based on the first 3 principal components (green star). The symbols show the model error scores for the first 2, 3, 5, and all principal components. As in Figure 3.1, top-performing models (Table 3.3) are highlighted in bold, and GFDL CM3 and ACCESS 1.0 GCMs are highlighted in blue.

precipitation metrics lead to a significantly different ranking from theirs (compare our Figure 3.2 with Figure 3 in Rupp et al. 2013). For example, there are only 5 models that rank within the top 15 GCMs in both evaluations (CanESM2, CESM1-WACCM, EC-EARTH, IPSL-CM5A-MR, HadGEM2-ES).

Another result highlighted in Brekke et al. (2008) is that once at least 6-10 models are included in an ensemble, the average projection is not strongly dependent on which specific models are used to calculate the average. However, this does not address the impact of model selection on the *range* among projections. As illustrated in the following section, the range among projections can be significantly affected by the choice of ensemble. Since the current study necessitates the selection of just two bracketing scenarios, the implications for the ensemble range is critical.

We took two steps intended to accurately represent the range among projections while also accounting for model fidelity to PNW climate. First, we selected a subset of top-performing models by eliminating those that performed the worst for the evaluation metrics listed in Table 3.2. Metrics were grouped in rough accordance with the principal components analysis and the worst-performing models in each category were excluded. Second, we retained a relatively large subset of models – 13, in total – in our final ensemble (Table 3.3), from which we selected two GCM projections for the RCM downscaling.

Retained	Excluded	Not Evaluated (missing data)
ACCESS1-0	bcc-csm1-1	EC-EARTH (RCP 4.5)
CanESM2	bcc-csm1-1-m	HadCM3 (RCP 4.5, RCP 8.5)
CESM1-CAM5	BNU-ESM	MRI-ESM1 (RCP 4.5)
CESM1-WACCM	CCSM4	
CNRM-CM5	CESM1-BGC	
GFDL-CM3	CESM1-FASTCHEM	
HadGEM2-AO	CSIRO-Mk3-6-0	
HadGEM2-CC	FGOALS-g2	
HadGEM2-ES	GFDL-ESM2G	
inmcm4	GISS-E2-R	
MPI-ESM-LR	GISS-E2-H	
MPI-ESM-MR	IPSL-CM5A-MR	
NorESM1-M	IPSL-CM5A-LR	
	MIROC5	
	MIROC-ESM	
	MRI-CGCM3	

Table 3.3. Results of the model evaluation. A total of 13 GCMs were selected for inclusion in the final ensemble. The two bracketing scenarios were selected from this final subset.

Greenhouse Gas Scenarios

"What if" Scenarios of Future Emissions

Greenhouse gas emissions are influenced by a wide range of complex social, political, and environmental factors (population growth, geopolitics, technological innovations, etc.). Needless to say, these factors are difficult to predict. Instead of trying to predict how these factors change in the future, researchers develop plausible "scenarios" of future greenhouse gas concentrations. Recognizing that there is more than one way to reach the same level of emissions – via different combinations of policy, technology, or other changes – recent work has emphasized selecting a small number representative scenarios and evaluating the different ways that these could be achieved.

The Representative Concentration Pathways

The Representative Concentration Pathways (RCPs, Van Vuuren et al. 2011), developed for the most recent Intergovernmental Panel on Climate Change assessment (IPCC 2014), were selected from the academic literature on future greenhouse gas emissions. The four RCPs were selected to span the range of plausible scenarios of future greenhouse gas concentrations, based on a comprehensive review of the literature on future emissions pathways. As with previous greenhouse gas scenarios, none of the RCPs was assigned an explicit likelihood.

New advances in global climate models allow them to capture carbon exchanges between the land, ocean, and atmosphere. This means that a different balance of fluxes can lead to the same atmospheric concentration of greenhouse gases. As a result, the new RCP scenarios specify greenhouse gas concentrations, which can be achieved via differing combinations of human and natural fluxes. In contrast, the previous generation of scenarios specified emissions.

Scenario selection

In RCP 2.6, emissions decline substantially in the early 21st century, radiative forcing peaks around the middle of the 21st century, and net emissions are near zero by 2100. In RCP 4.5, emissions decline substantially by the end of the 21st century and greenhouse gas concentrations peak prior to 2100. For RCP 6.0, emissions grow prior to 2050 but generally decline toward the end of the 21st century, and greenhouse gas concentrations peak after 2100. RCP 8.5 is the only scenario in which emissions are not stabilized in the 21st century and instead continue to grow throughout the 21st century.

In this study we use the RCP 4.5 and 8.5 scenarios to represent the low- and high-end of likely future emissions (IPCC 2014, Clark et al. 2014). We omitted the RCP 2.6 scenario because recent research suggests it would require aggressive near-term global emissions reductions than are likely infeasible. Specifically, Davis and Socolow (2014) estimate the "committed emissions" given the expected lifetime of current fossil fuel

Current scenarios	**Concentration in 2100 (ppm CO_2-eq)**	**Change in annual CO_2-eq emissions (% of 2010 emissions)**		***Description***
		2050	**2100**	
RCP 2.6	430-480	-72 to -41%	-118 to -78%	*"Very Low"*
RCP 4.5	580-720	-38 to +24%	-134 to -21%	*"Low"*
RCP 6.0	720-1000	+18 to +54%	-7 to +72%	*"Moderate"*
RCP 8.5	>1000	+52 to +95%	+74 to +178%	*"High"*

Table 3.4. The latest set of greenhouse gas scenarios are called Representative Concentration Pathways (RCPs, Van Vuuren et al. 2011). The table shows the target concentration in 2100 and the percent change in annual emissions, relative to 2010, for both 2050 and 2100. Both are expressed in "CO_2-equivalent", in which the global warming potential of all greenhouse gases is expressed in terms of the equivalent amount of CO_2. *Source:* IPCC 2014.

infrastructure. Building on this work, Pfeiffer et al. (2016) estimate that these commitments would grow to exceed the 2°C global warming target (which RCP 2.6 was designed to represent) by the year 2017. In other words, according to the Pfeiffer et al. analysis, the 2°C target could only be met if either (a) no new fossil fuel infrastructure is constructed after 2017, or (b) if existing infrastructure is retired early or retrofitted to capture enough carbon emissions to compensate for any new development.

In contrast with RCP 2.6, existing research suggests that the RCP 4.5 scenario is still a potentially feasible target for emissions through 2100. Specifically, Riahi et al. (2014) find that both the cost and feasibility of remaining below a target concentration of 550 ppm CO_2-eq by 2100 (which is lower than the RCP 4.5 target) is virtually unaffected by emissions before 2030. In other words, the delay in global emissions reductions does not preclude achieving an emissions trajectory that is consistent with the RCP 4.5 scenario. Similarly, Pfeiffer et al. (2016) estimate that continued investments in fossil-fuel intensive infrastructure would not commit the world to a 50% chance of exceeding RCP 4.5 until the year 2042.

Nonetheless, the significance of the required emissions reductions should not be understated. For example, Rozenberg et al. (2015) estimate that achieving RCP 4.5 would require a 25-50% decrease in the average carbon intensity (carbon emissions per unit energy) of new energy production, averaged over the period 2014-2050, relative to its 2010 value. Capellán-Pérez et al. (2016) estimated that there is an 8% chance that future emissions remain below the RCP 4.5 target by 2100. In addition, the IPCC report emphasizes that (1) near-term delays in emissions reductions require steeper cuts in the future to meet a particular greenhouse gas concentration target, and (2) near-term investments in technology and institutional capacity are needed in order to ensure that long-term reductions in emissions remain feasible. To summarize: recent emissions, and even those for the next 1-2 decades, do not preclude the RCP 4.5 scenario. However, the longer that global emissions continue to grow, the less likely it becomes that the RCP 4.5 scenario will be achievable.

RCP 8.5 is often referred to as the “business as usual” scenario, since its growth in emissions is most similar to the experience of the past few decades. However, some recent work (e.g., Capellán-Pérez et al. 2016; Ritchie and Dowlatabadi, 2018) has shown that global emissions may not grow as quickly as suggested by the RCP 8.5 emissions trajectories. This suggests that RCP 8.5, as intended, is representative of the high end of plausible emissions through 2100 – just as RCP 4.5 likely represents the low end of feasible emissions. Nonetheless, there is one important way in which RCP 8.5 is distinct: greenhouse gas emissions will not end in 2100. Since RCP 8.5 represents a scenario in which emissions do not stabilize by 2100, greenhouse gas concentrations would very likely still reach the RCP 8.5 targets – even if not by 2100.

GCM Selection

Given a selection of top-performing models (Table 3.3) and a choice of greenhouse gas scenarios, the next task was to select the two GCM projections to be used as boundary

conditions for the RCM simulations. Based on consultation with King County, we chose to select models that bracket the range of future changes in extreme precipitation. Specifically, GCM selection consisted of identifying a model showing large increases in extreme precipitation, coupled with a high greenhouse gas scenario (RCP 8.5), and comparing this to a model showing small or negative changes in extreme precipitation and a low greenhouse gas scenario (RCP 4.5). We refer to these as the "High-High" and "Low-Low" scenarios, respectively.

As noted above, the two models were selected based on projected changes in extreme precipitation. Although the model ranking was motivated by concerns over the utility of precipitation estimates from global models, projected changes in precipitation were nonetheless used as a proxy for model selection. This is undoubtedly an imperfect approach to model selection, but was deemed the best approach for approximating local changes in extremes. As outlined below and in Lorente et al. (2018), additional research is needed in order to develop statistical relationships between large-scale conditions and local variations in precipitation extremes.

To evaluate differences among precipitation extremes – a key focus of this study – we used historical and future precipitation extreme indices from the Expert Team on Climate Change Detection and Indices (ETCCDI; Sillman et al. 2013a, 2013b; Table 3.5). These variables were available for most of the models listed in Table A.1, and have been used as extreme indices in a variety of case studies for observed and projected changes in extreme precipitation events (Kenyon and Hegerl, 2010; Westra et al, 2013; Fischer and Knutti, 2014).

Figures 3.3 and 3.4 compare GCMs projections in terms of projected 21st century changes in climate. We focused on the results for the 2080s for the model selection, and sought to identify models that were consistently ranked at the low or high end of the range. Based on these criteria, we selected two CMIP5 model-scenario pairs – ACCESS 1.0, RCP 4.5 ("Low-Low") and GFDL CM3, RCP 8.5 ("High-High") – for use in driving the RCM simulations (Table 3.6).

ID	*Indicator name*	*Definition*	*Units*
R95p	Very wet days	Annual total precipitation when PRCP>95th percentile (calculated over the 1961-1990 period)	mm
R99p	Extreme wet days	Annual total precipitation when PRCP>99th percentile (calculated over the 1961-1990 period)	mm
Rx1day	Max 1-day precipitation amount	Seasonal/annual maximum 1-day precipitation	mm
Rx5day	Max 5-days precipitation amount	Seasonal/annual maximum 5-day precipitation	mm

Table 3.5. Extreme precipitation indices obtained from the Expert Team on Climate Change Detection and Indices (ETCCDI, Sillman et al. 2013a, 2013b).

The validation shows that these two models are well within the typical range of performance among global climate models and perform better than most GCMs for precipitation-related metrics (Figures 3.1 and 3.2). In terms of the projections, Figures 3.3 and 3.4 show that the two models represent the high- and low-end of projected changes in winter precipitation, particularly in terms of the extremes. Temperature changes projected by the two models are well within the range of other CMIP5 model projections.

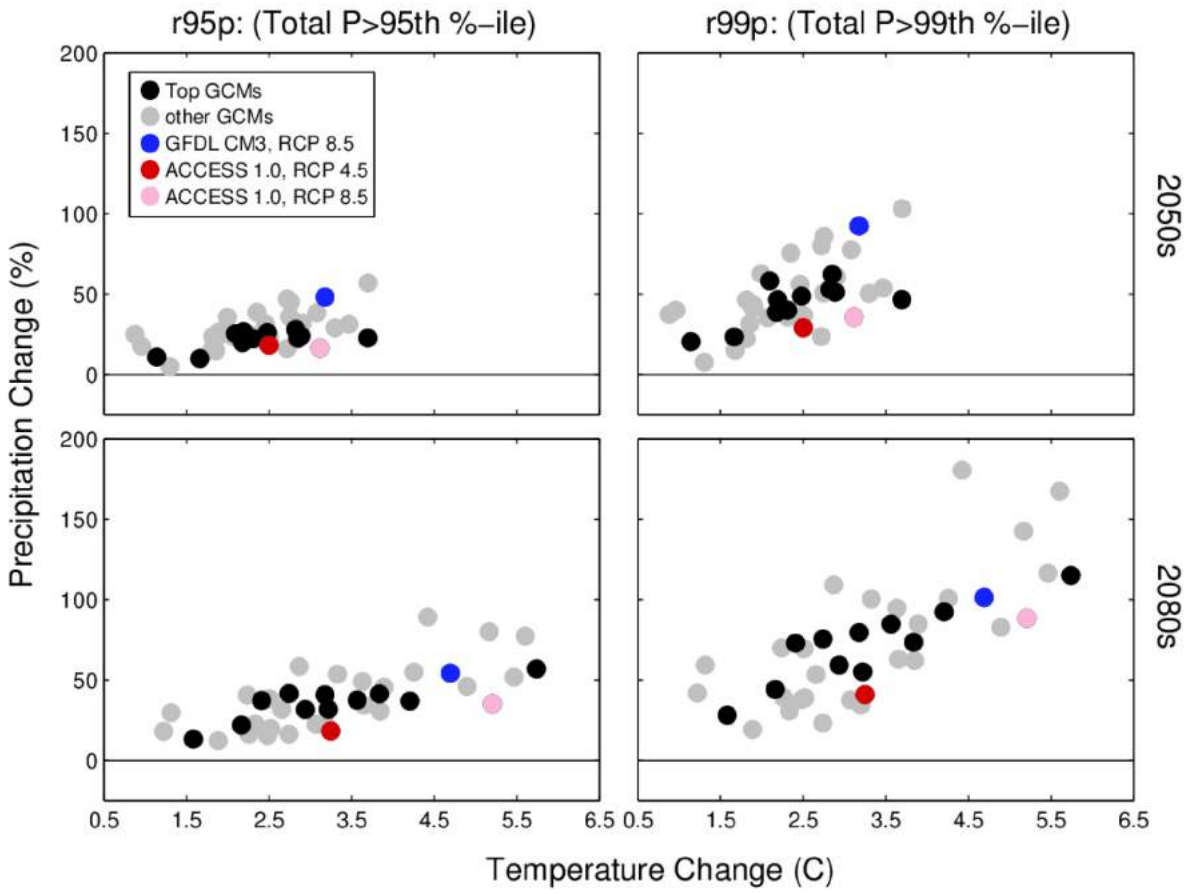

Figure 3.3. Projected changes in temperature and precipitation for the CMIP5 based on both the RCP 4.5 and 8.5 scenarios. Annual average temperature change is shown on the x-axis of each plot, while the y-axes show the percent change in two metrics of extreme precipitation: r95p (left), and r99p (right, Table 3.5). The top row shows the results for the 2050s; results for the 2080s are shown in the bottom row. Results for both the RCP 4.5 and 8.5 scenarios are included in each plot. The top GCMs identified in the evaluation are highlighted in black, while results for the remaining models are shown in gray. The GFDL CM3 projection for the RCP 8.5 scenario (blue) was selected to represent the high end of extreme precipitation projections, while the ACCESS 1.0 projectoin for the RCP 4.5 scenario (red) was selected to represent the low end of extreme precipitation projections. For reference, the RCP 8.5 scenario for ACCESS 1.0 is highlighted in pink, though it was not selected for the RCM simulations. The RCP 4.5 scenario for GFDL CM3 was not available from ETCCDI at the time of this writing. Similarly, ETCCDI indices were not available for some of the other models included in the GCM evaluation.

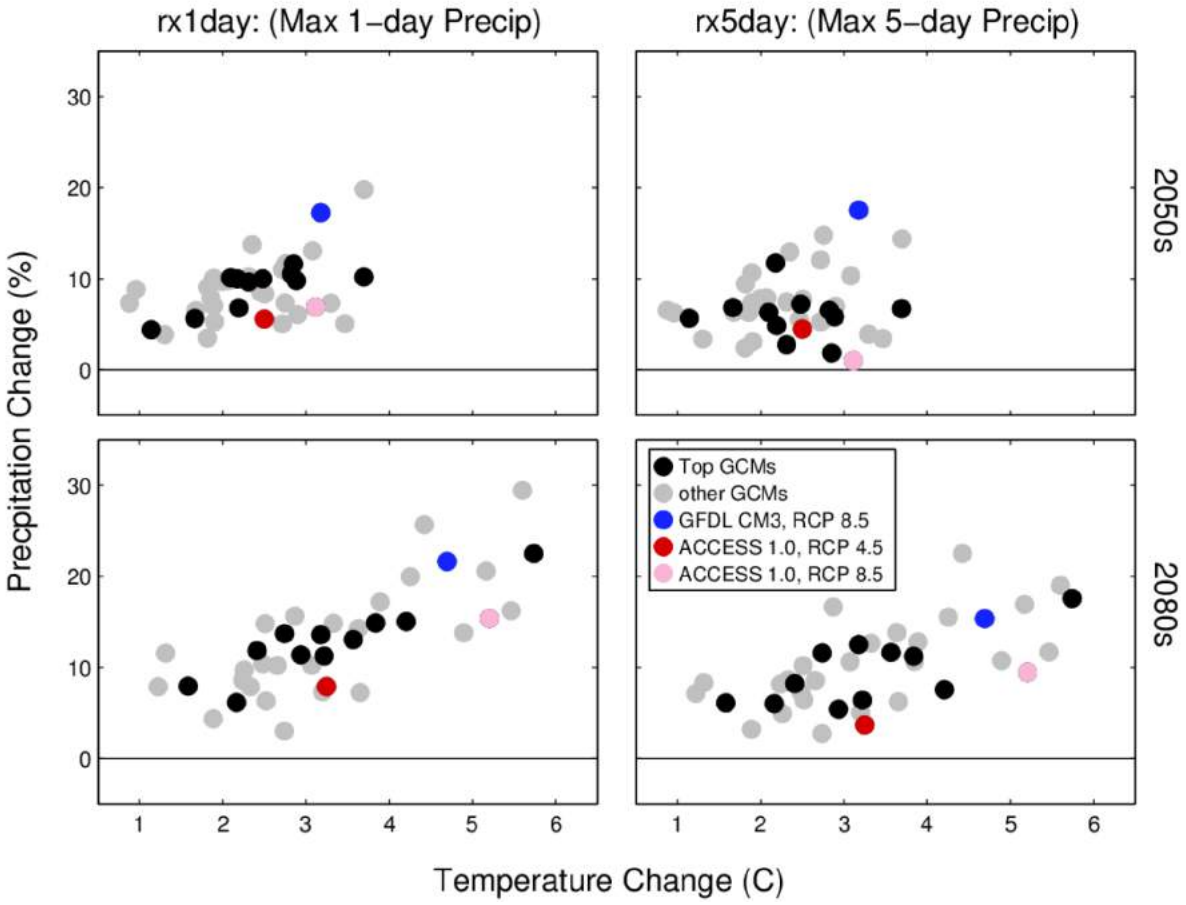

Figure 3.4. As in Figure 3.3 except showing results for rx1day and rx5day.

Table 3.6. Model-Scenario pairs for the two global projections used to drive the regional model simulations. "Model" refers to the Global Climate Model (GCM), while "Scenario" refers to the greenhouse gas scenario (Van Vuuren et al. 2011, for more information see Chapter 1 of Mauger et al. 2015). These were chosen to bracket the range from a low-sensitivity model driven by a low-end greenhouse gas scenario ("Low-Low") to a high-sensitivity model driven by a high-end greenhouse gas scenario ("High-High").

Model	***Model Citation***	***Greenhouse Gas Scenario***	***Shorthand Description***
ACCESS 1.0[*]	*Griffies et al. 2011*	*RCP 4.5 (Low emissions)*	"Low-Low"
GFDL CM3[†]	*Bi et al. 2013*	*RCP 8.5 (High emissions)*	"High-High"

[*]Australian Community Climate and Earth System Simulator coupled model, version 1.0
[†]Geophysical Fluid Dynamics Laboratory Climate Model version 3

4 Statistical-Dynamical Downscaling

Recent research has demonstrated that current statistical downscaling approaches do not adequately capture changes in precipitation extremes, thereby necessitating new dynamically downscaled projections to quantify changes in heavy rain events (e.g., Salathé et al. 2014). However, it is possible that robust statistical relationships exist between the large-scale weather conditions that are well simulated by global models and the local-scale implications for precipitation extremes. A statistical approach would allow us to evaluate changes in heavy precipitation across a large ensemble of global models and greenhouse gas scenarios without having to take on a large number of computationally expensive RCM runs.

In this study we took two approaches to exploring the feasibility of developing a statistical model linking large-scale dynamics to local scale precipitation extremes. In both cases we used three existing Weather Research and Forecasting (WRF, Skamarock et al. 2005) simulations in order to proceed with the research in parallel. These were forced by the following global climate datasets:

1. NCEP-NCAR reanalysis project (NNRP, Kalnay et al. 1996, 1950-2010).
2. ECHAM5 global model (Meehl et al. 2007), A1B greenhouse gas scenario (1970-2070).
3. CCSM3 global model (Roeckner et al. 2003), A1B greenhouse gas scenario (1970-2070).

The first was used as a proxy for observed precipitation; previous validation studies show that this is a reasonable assumption (e.g., Dulière et al. 2011). Using the NNRP-WRF simulation allows us to reliably evaluate the spatial distribution of precipitation while also ensuring a direct correspondence between the large-scale global fields and local precipitation intensities. The other two simulations were used to evaluate projected changes in precipitation extremes.

The following two sections describe two analyses aimed at identifying the drivers of heavy precipitation in the Pacific Northwest and evaluating whether or not these drivers are projected to change.

Diagnosing Changes in Large-Scale Dynamics

In the first approach we examined the daily rain rate and Integrated Vapor Transport (IVT) associated with each mode by regressing the full fields onto the combined Empirical Orthogonal Functions (EOFs) for each mode (Mauger et al. 2016). IVT measures the flux of water vapor through an atmospheric column, calculated by adding up the product of water vapor and winds at each level in the atmosphere.

Approach

From a large-scale perspective, precipitation is a consequence of converging water vapor – i.e., if you accumulate enough water vapor in an area, at some point it will rain. Previous research suggests that precipitation during high intensity events is largely governed by the amount of water vapor that is being transported into the region (Warner et al. 2015), as opposed to dynamical factors such as the depth of the low pressure or the direction of winds. In contrast with precipitation, water vapor transport is well resolved by global models. As a result, we focused our analysis on the daily mean total precipitable water vapor (TPW, column-integrated water vapor) and integrated vapor transport (IVT, mass-weighted average vapor flux). Since IVT is a flux term, it includes both a zonal (East-West) and a meridional (North-South) component.

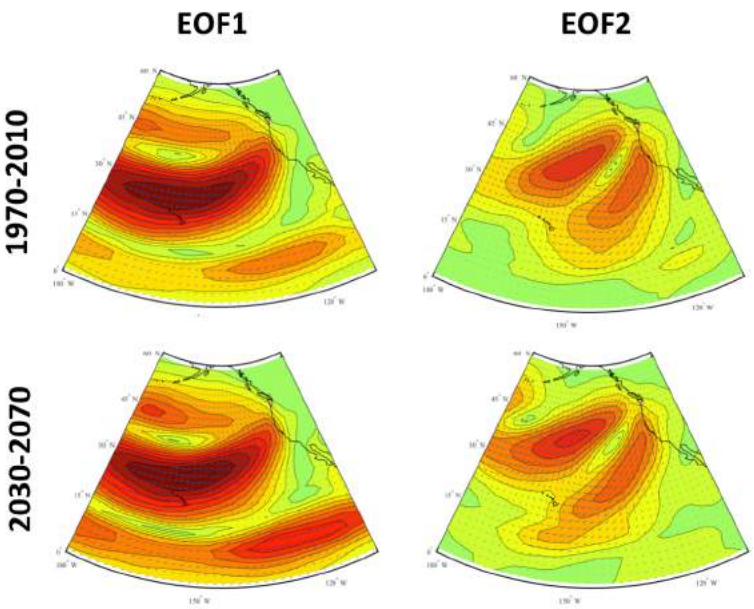

Figure 4.1. Composite anomaly in integrated vapor transport (IVT) for the 1st and 2nd modes identified in the EOF analysis. Results are shown for the ECHAM5 model for historical (1970-2010) and future (2030-2070); similar patterns were found for the other WRF simulations. No color scale is shown because these are normalized anomalies: red shading indicates above average conditions, while the light green shading indicates average conditions. Wind vectors are denoted with arrows.

Principal components analyses (often referred to as Empirical Orthogonal Functions, or EOFs) were explored to identify the primary modes of IVT spatial variability associated with heavy precipitation events over the basin. Both a combined EOF and a complex EOF analysis were performed on the global model daily IVT fields. A combined EOF identifies the primary modes of variability in IVT associated with maximum variance in the combined zonal and meridional components of the vapor transport resulting in separate spatial patterns for the IVT components (the EOFs) based on their in-phase maximum variance. A complex EOF is similar to a combined EOF, but the maximum variance in the zonal and meridional winds associated with the primary modes of variability are not necessarily in-phase with one another. Because the complex EOF approach maximizes the variance in the transport components regardless of their phase, it is potentially a better approach for exploring the impact of any change to the path of AR events impinging on the region, either due to changes in the latitude of the storm track or its angle relative to the coastline.

We performed an EOF analysis on daily IVT data for only those days when the daily precipitation was at or above the 90th percentile for that grid point. The 90th percentile was chosen as a compromise between increased sample size and the need to focus on high intensity rain events. Prior to calculating the combined EOF the two integrated transport

terms, IQU (zonal) and IQV (meridional), were standardized (i.e., by removing the mean and dividing by the standard deviation). The complex EOF is based on performing a single value decomposition of the complex matrix:

$$Z = IQU' + i \cdot IQV'$$

where IQU' and IQV' are the normalized anomalies, as defined as above. The real part of the complex EOFs are the spatial patterns associated with the zonal vapor transport, while the imaginary part of the complex EOFs are the spatial patterns associated with the meridional vapor transport. Similarly, the real part of the complex PCs represents the time variability of the modes for the zonal vapor transport, while the imaginary part of the complex PCs represents the time variability for the meridional vapor transport.

Results

We applied the EOF analysis separately to the global model IVT data based on 90th percentile precipitation events for each of the historical WRF simulations (NNRP, ECHAM5, CCSM3). Each set of EOFs consistently showed two leading modes of variability (Figure 4.1). The dominant mode shows the typical pattern one might expect for these events, with southerly or southwesterly flow associated with a mid-latitude cyclone intercepting the coastline, while the second shows the alternate configuration, in

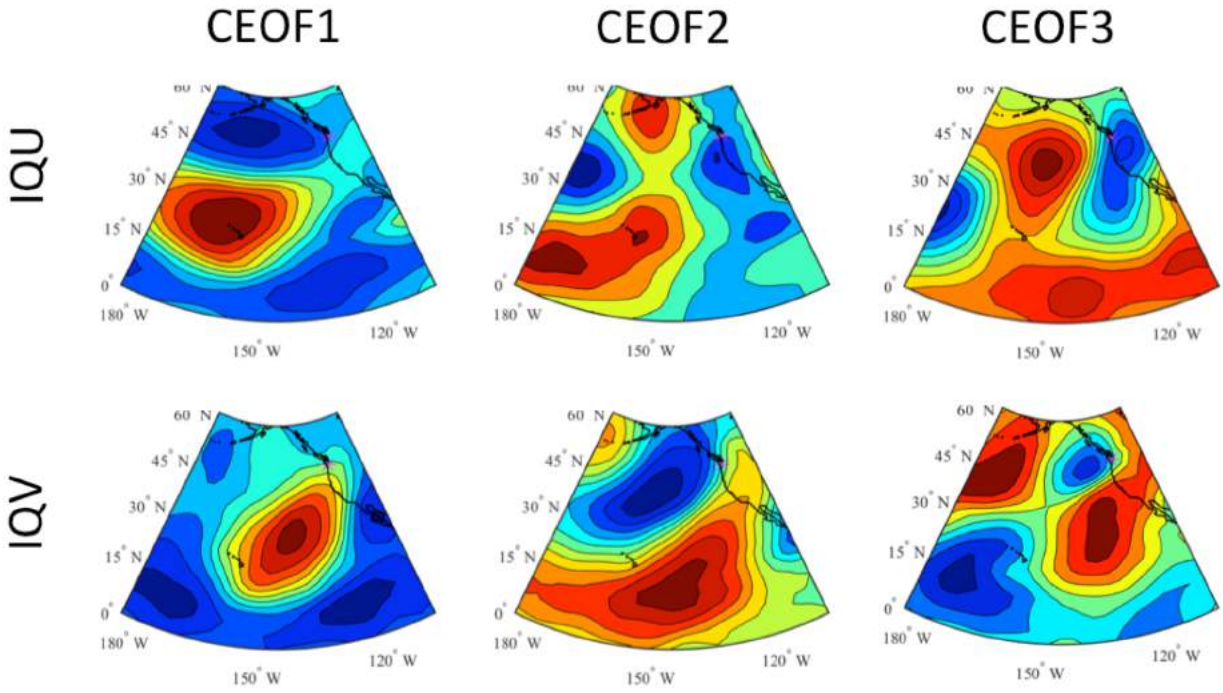

Figure 4.2. Composite anomaly in integrated vapor transport (IVT) for the 1st 2nd, and 3rd modes identified in the complex EOF analysis. Results are shown for the NNRP simulation model for 1970-2010; similar patterns were found for the other WRF simulations. Since it is a complex EOF, both westerly (IQU) and southerly (IQV) integrated vapor transport are shown for each mode. No color scale is shown because these are normalized anomalies: red shading indicates positive anomalies (anomalous westerly or southerly transport), while blue shading indicates negative anomalies (anomalous easterly or northerly transport).

which the flow is influenced by anti-cyclonic circulation also associated with a wave in the jet stream (referred to as Rossby waves). Both are well-known atmospheric river event configurations for the Pacific Northwest (Ryoo et al. 2013). There is also a third pattern (not shown) that appears distinguishable from the noise in some analyses, and which may be associated with a smaller cyclone breaking downstream of a larger system over the Pacific – this third mode would require more study to understand its development. Although all analyses show the same sequencing among the first few modes, the decrease in variance explained for the 2nd and 3rd modes is greater for the global model simulations (ECHAM5, CCSM3) than for the observationally-based reanalysis simulation (NNRP). In all analyses, the first mode explained about 10-20% of the variability, while the 2nd and 3rd modes explained about 7-10% of the variability each.

The combined EOF analysis was also applied to the future simulations for the years 2030-2070. These showed the same modes, but with more water vapor transport. This is consistent with previous research (Warner et al. 2015, Scheff et al. 2015), which suggests that changes in precipitation in the Pacific Northwest are primarily driven by the increase in water-holding capacity of warmer air and not with a change in the intensity or position of storm systems. All of these future modes explain a smaller proportion of the variability than in the historical period.

Anomalies in each variable associated with the zonal (IQU) and meridional (IQV) vapor transport modes must be examined separately in the case of the complex EOF analysis since the phase of their maximum variance differs (Figure 4.2). This analysis shows that the transport anomalies in the zonal direction are first, followed by the transport anomalies in the meridional direction. To complete a full phase of the wave captured by the complex EOF analysis, the negative of the zonal transport pattern would then occur, followed by the negative of the meridional transport pattern (only the positive patterns are shown in Figure 4.2). In the case of the first mode, the anomalous westerly transport anomalies (red) across the Pacific centered on about 20°N accompanied by the anomalous easterly transport (blue) to the north are followed by anomalous southerly transport reaching from south of Hawaii to the west coast of North America. These anomalies describe a mid-latitude cyclone circulation like that seen for the first combined EOF mode in Figure 4.1. In general, the two leading complex modes correspond closely with those identified in the combined analysis, in addition to a more robust third mode that appears to lack the clear atmospheric river signal seen in the previous two patterns. As with the combined analysis, the global model projections assigned more weight to the leading EOF relative to the reanalysis-based simulation.

Evaluating the time progression of WRF rainfall associated with the complex EOF patterns, maximum rainfall anomalies are observed in association with the westerly vapor transport anomalies a day after the maximum anomalies in the southerly vapor transport. This is consistent with the fact that the westerly vapor transport anomaly maximum over the basin occurs after the low pressure center has arrived onshore, whereas the southerly transport anomaly is a maximum as the storm first arrives at the coast.

For both the combined and complex EOF analyses the primary modes of variability in IVT are associated with an AR event linked to a mid-latitude wave-like structure in the storm

track. Neither analysis indicated substantial variation in the angle at which these events intercept the coastline: as shown in Figure 4.1, the moisture transport consistently arrived from the south or south-southwest. However, more study is required to examine the transport vectors in order to fully understand the implications of the transport directional anomalies and precipitation in the basin.

This analysis suggests that the mechanisms driving heavy rain events are not expected to change substantially in the future. However, as in previous research (e.g., Warner et al. 2015), the projections do show an increase in moisture transport during large storm events. This analysis did not consider other factors that could affect precipitation over the region, including atmospheric stability, vertical velocity, or the origin of AR airmasses.

Comparing Heavy Rain Events in Puget Sound and the Outer Coast

The previous analysis evaluated the dominant mechanisms driving heavy precipitation in the Pacific Northwest as a whole. That analysis indicates that a parameterization based on offshore vapor transport could have some skill in representing the resulting precipitation on the coast and inland. However, a number of challenges remain, including (1) potential differences in the mechanisms leading to heavy rainfall across the region, and (2) how to statistically represent the relatively localized nature of AR precipitation. In this second study we emphasize the first question – what are the coherent modes of precipitation variability, and how do the large scale conditions change for each? The following provides a brief summary of the analysis, which is discussed in greater detail in Lorente et al. (2018).

Approach

We begin by using WRF precipitation fields to identify areas of coherent variability. Our analysis is focused on the western part of the 12-km domain (defined by the crest of the Cascade Range) in order to reduce computational time and because of ambiguity about the role of ARs and the ability of the model to accurately represent them in the eastern part of the domain.

First, an EOF analysis is applied to the time series of mean daily precipitation. We use covariances, as opposed to correlations, in order to emphasize extreme events in the EOF analysis. By taking only the first few modes, the EOF analysis effectively reduces the amount of noise in the precipitation field. Next, a clustering analysis is used to group daily precipitation time series based on the Euclidean “distance” between grid cells:

$$d_{ij} = \frac{1}{M}\sqrt{\sum_{k=1}^{M}(e_k(x_i) - e_k(x_j))^2}$$

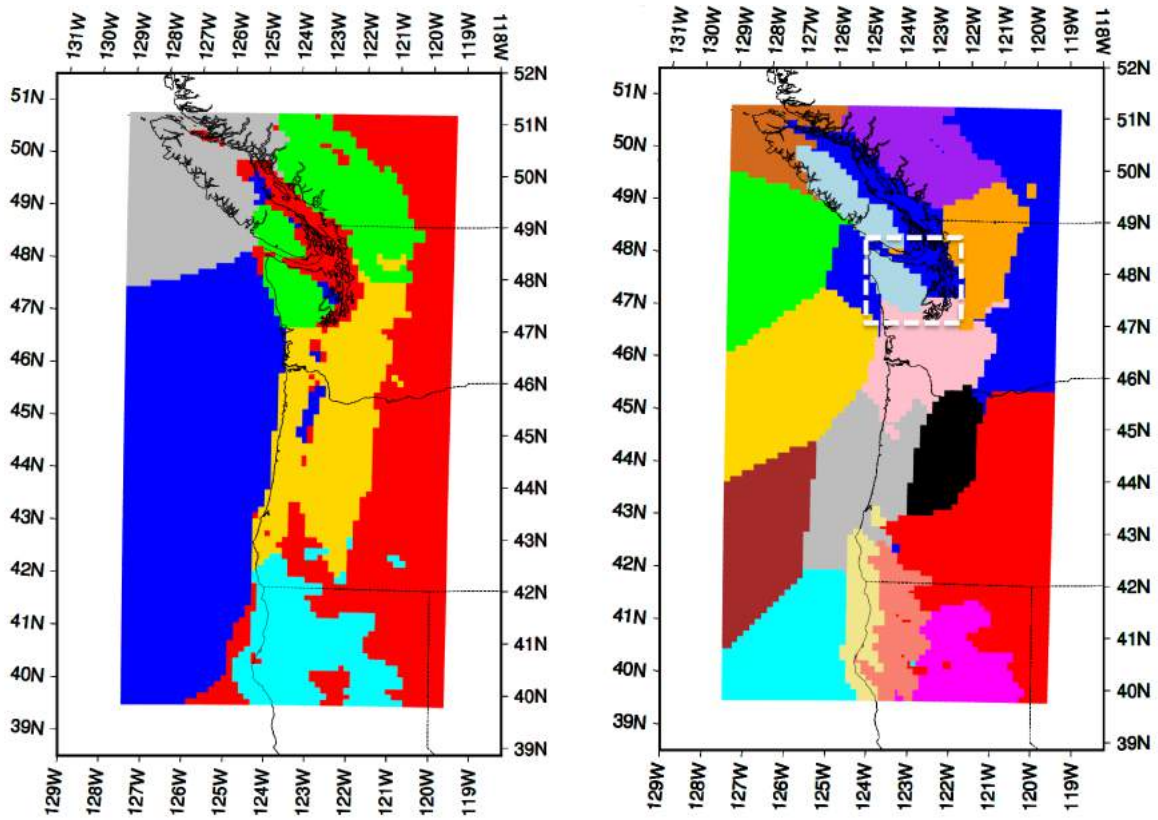

Figure 4.3. Regions with different temporal variability obtained in the clustering analysis using daily precipitation from October to March. Clustering methods are applied to 5 empirical orthogonal functions (EOFs) obtaining 6 regions (left) and to 20 EOFs obtaining 16 regions (right). The white rectangle shows the focus region for this study.

where $e_k(x)$ is the value of the k^{th} retained eigenvectors at grid point x, including all M retained EOFs according to the scree plot test. The distance (d_{ij}) represents the similarity between two precipitation time series at the grid points x_i and x_j. Lower values of d_{ij} indicate similar temporal variability.

We employ a two-stage clustering algorithm combining hierarchical and non-hierarchical algorithms (Kaufman and Weber 1996). Hierarchical clustering using Ward's minimum variance Ward (1963) provides the centroids of the first-guess cluster which are used as initial seeds for the K-means non-hierarchical method (Wilks 1995). These methods are applied to the retained modes using the distance metric d_{ij}.

The clustering identifies a number of coherent regions of variability in western Washington and Oregon (Figure 4.3). Two particularly robust regions are the western slopes of the Olympics and the Puget Sound lowlands. In order to compare precipitation variability in these two regions, we construct a single time series of daily cool-season (October to March) precipitation for the Olympic Mountain and Puget Sound regions by averaging over all grid cells in each region for the last 40 years of the WRF NNRP simulation (1970-

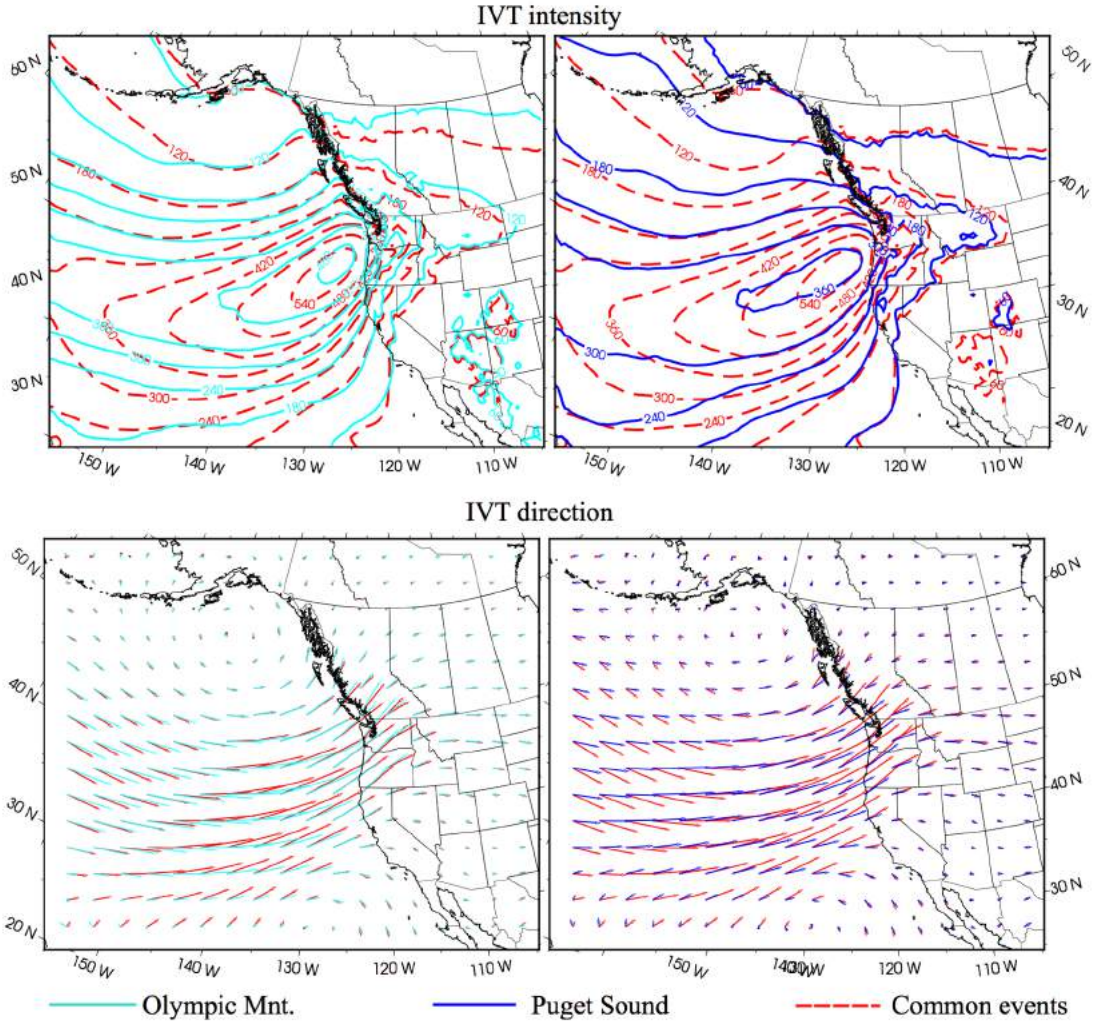

Figure 4.4. IVT intensity (first row) and IVT direction (second row) composites during extreme precipitation events in the Olympics (first column, cyan) and Puget Sound (second column, blue). In all plots, results for the Common events are shown in red.

2010). Since these regions are identified through the cluster analysis, the regional time series are generally well correlated across each of the grid cells in the region.

Extreme precipitation events were identified according to the 95th percentile of each time series, and days with precipitation that exceeds this threshold are hereafter referred to as "extreme events." This corresponds to the 375 days with heaviest precipitation in each region. Similar results were obtained with a more restrictive threshold of 99th percentile. The extreme event days were then used to create composites of the large scale conditions associated with extremes for each region: integrated vapor transport (IVT), integrated water vapor (IWV), and 850 hPa winds over the larger 36-km domain.

The 95th percentile in daily precipitation is 13.7 mm for Puget Sound and 55.0 mm for the Olympic Mountains (about 0.5 inch and 2 inches, respectively). Of these events, 63% occurred on the same day in both regions (hereafter termed "Common events"), and 37%

were unique to each region (hereafter referred as either “Puget Sound” or “Olympic Mountain” events).

Figure 4.4 shows the IVT for days with extreme events in Puget Sound (blue), the Olympic mountains (cyan) and in both regions (red). For each set of extreme events, spatial patterns of IVT composites are similar, with larger values between 25 and 35 latitude, and a maximum close to the coast. Large values of IVT penetrate inland as far east as Montana in all cases. The largest IVT, in excess of 540 kg/m/s, occurs during Common extreme events (red). IVT during Puget Sound events exhibits a weaker latitudinal gradient. High values of IVT originate deeper into the subtropics during the Common events, extending below 30°N latitude. This southerly extent of the Common events is made even more clear in the analysis of the IVT vectors (second row), which show the IVT plume for Common events extends from 25°N to the Pacific Northwest, originating in a region of substantially warmer sea surface temperatures. The Olympic events likewise extend into the subtropics, but not as far. In contrast, the Puget Sound events are associated with a more zonal (westerly) moisture flow across the relatively cooler North Pacific. The more southerly winds for Olympic and Common events suggest the transport of warmer air masses during these events is a critical feature, whereas it is not as dominant for the events that manifest only in Puget Sound.

To better assess the differences between Olympic and Puget Sound events, Figure 4.5 shows the difference maps (Puget Sound minus Olympics) for IVT, IWV and wind speed at 850 hPa. The differences are normalized to facilitate side-by-side comparisons. IWV is larger over Alaska and the North Pacific during Puget Sound events, but there are no significant differences where IVT is larger, below 45°N. In contrast, the anomalies for 850 hPa winds are more distinct. An increase of 48% can be found close to the coast, in the same locations as the peak in IVT. This suggests that IVT differences between Olympics and Puget Sound are associated with changes in the dynamics as opposed to differences in moisture transport.

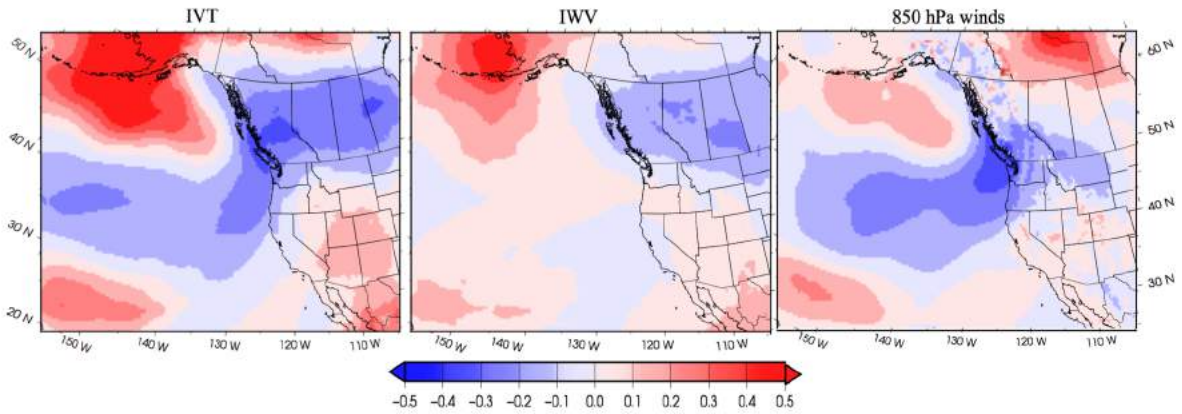

Figure 4.5. Normalized difference – Puget Sound minus Olympics events – for IVT (left), IWV (middle) and 850 hPa wind speed (right).

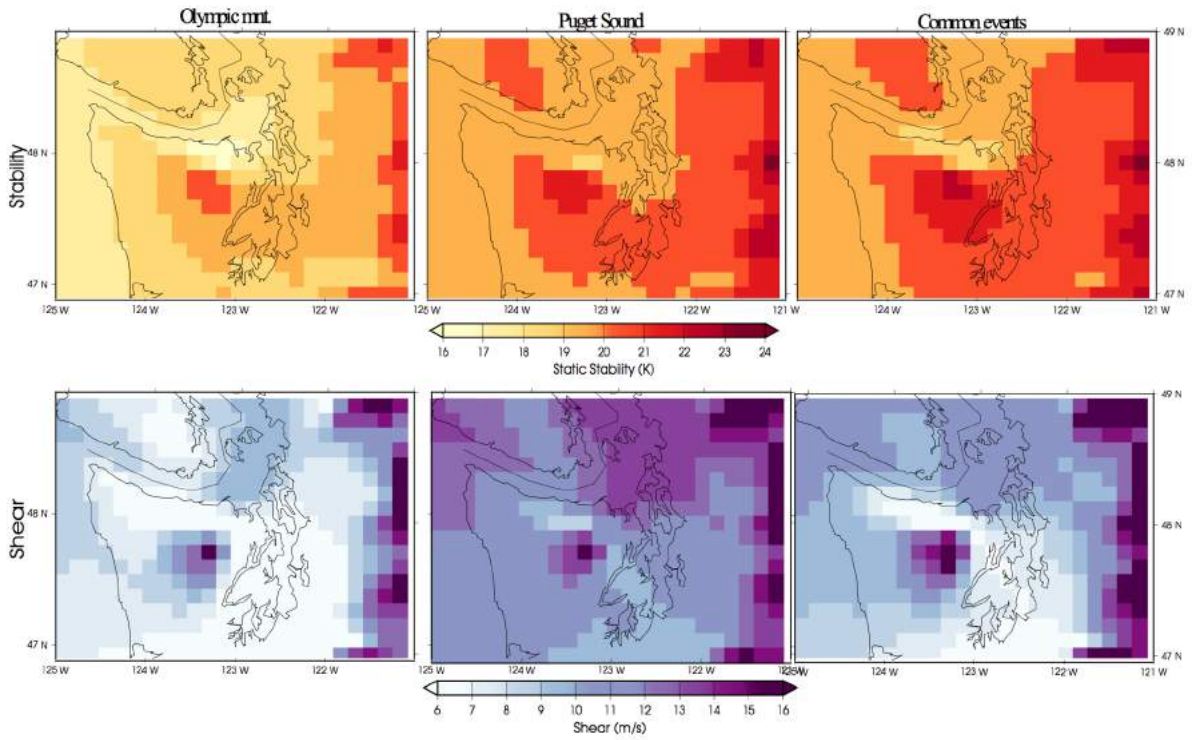

Figure 4.6. Static stability (first row) and wind shear (second row) during Olympics (left), Puget Sound (middle) and Common regions (right) using the 12 km WRF domain over western Washington State.

Although it appears that winds, and therefore the dynamics, are the primary determinant of differences between Puget Sound and Olympic events, it is possible that static stability or wind shear may also play an important role. Figure 4.6 shows the composites of the static stability ($\Theta_{500} - \Theta_{850}$) and wind shear ($\mathrm{WSPD}_{500} - \mathrm{WSPD}_{850}$) for the top precipitation events in each category. Stability is greatest for the Common and Puget Sound events, and much less pronounced for the Olympic Mountain events. For Puget Sound events, the increased stability extends over the Puget Sound region. During extreme events, wind shear increases along the core of enhanced IVT, and seems to be greatest during Puget Sound events.

Wind shear and stability affect vertical mixing and convection associated with evaporation (from descent) and condensation (from ascent). Figure 4.7 shows the vertical velocity (w) at 500 hPa and 850 hPa. All three event categories show windward ascent (orange) and leeside descent (purple). However, vertical velocities are much weaker for the Common events. In addition, the 500 hPa results show descent air (purple) over the Cascade and Olympic Mountains for the Common events.

This evidence suggests that the flow is more affected by the topography during Puget Sound and Olympics events. During the Common events, in contrast, the effect of topography appears to be much weaker, suggesting that large-scale precipitation could be more important than convective precipitation during these events.

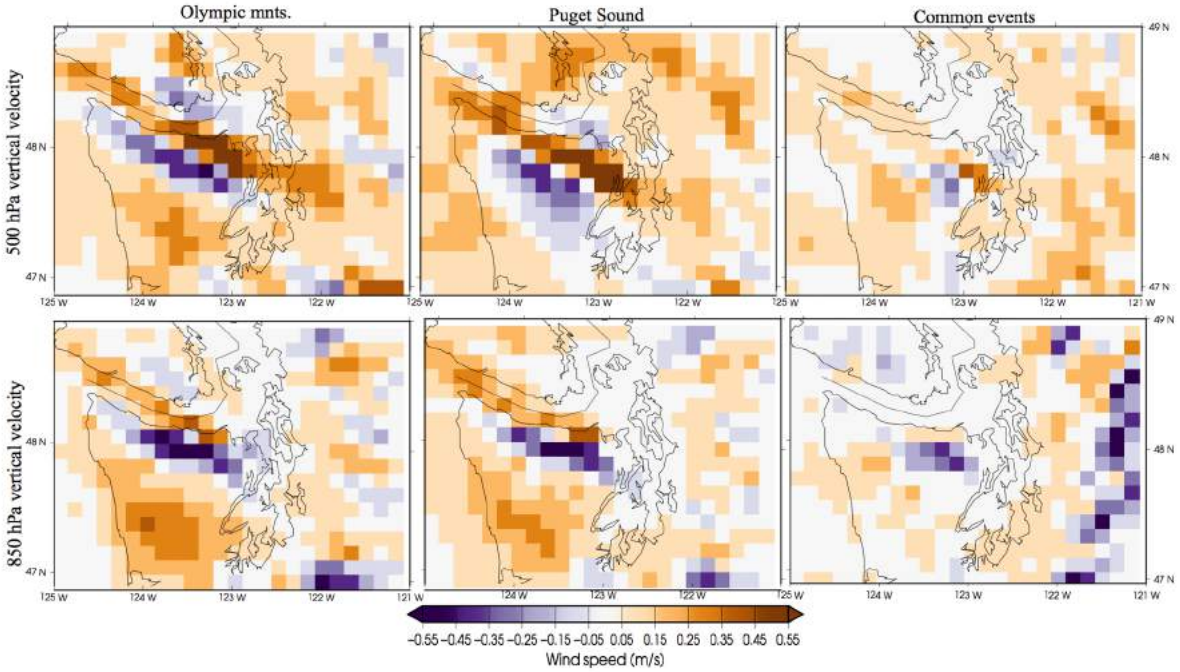

Figure 4.7. Vertical velocity at 500 hPa (first row) and at 850 hPa (second row) during Olympics (left), Puget Sound (middle) and Common events (right).

The findings also show that the Olympics events in particular are more influenced by convective precipitation as opposed to precipitation that results from large-scale uplift. Convective precipitation, since it results from localized updrafts, exhibits a much stronger rain shadow. In contrast, convective precipitation is relatively less important for the Common events, and these events exhibit a much weaker rain shadow. Results also indicate that the veering of winds with height leads to relatively warmer advection for the Common events, which serves to further decouple the precipitation from the topography.

One alternative possibility is that the Puget Sound events are “convergence zone” events, in which precipitation is enhanced in the lee of the Olympics due to the convergence of flows that are bifurcated by the Olympic Mountains. The more westerly flow for the Puget Sound events is consistent with observed incidences of convergence zone events (Mass 1981). However, these events would have lower stability due to the convergence, which is not consistent with Figure 4.6. Although there may nonetheless be some convection driven by downstream flow convergence, the results suggest that a weak rain shadow is the dominant feature of extreme events unique to the Puget Sound region.

Summary

For strong precipitation events (top 5% of daily cool-season events) over the Olympic mountain and Puget Sound regions, approximately 2/3 occur simultaneously while 1/3 are unique to each region. Although substantial research has been devoted to understanding the mechanisms driving the incidence of atmospheric rivers in the region,

relatively little is known about what makes these events different for specific parts of the Pacific Northwest.

We find that the Common events are associated with very strong atmospheric river patterns with deep off-shore troughing and substantial integrated water vapor transport extending from the subtropical Pacific to the Pacific Northwest.

The Olympic mountain events are similar to the Common events, sharing the atmospheric river structure, but with a less pronounced trough on average, lower levels of IVT, and a stronger rain shadowing. These events show more pronounced static instability than the Common events, which are fairly neutral. Such conditions favor strong rain shadows, with uplift and descent following the terrain.

Puget Sound events have more zonal flow and higher static stability than the Common events. These results suggest two mechanisms for increased heavy precipitation in the Puget Sound region: (1) Increased stability over the Puget Sound region, allowing large-scale uplift to persist in the lee of the Olympics (Siler et al. 2016), and (2) The westerly flow permits greater moisture transport through the terrain gaps north and south of the Olympic Mountains, supplying precipitation in the region, potentially with a Puget Sound Convergence Zone (Mass 1981). While the first mechanism is more consistent with our analysis, it is possible that both sorts of events are found in this category.

Synthesis

We analyzed heavy rain events from two perspectives. In the first approach we diagnosed the large-scale patterns associated with heavy rain events in western Washington, confirming that these are closely associated with an atmospheric river pattern. Performing the same analysis on the projections, we found that future events are driven by very similar large-scale conditions. It is possible that the projections showed a slight change in the position, intensity, or angle of the atmospheric river events, but overall the patterns were very similar. This is consistent with previous research indicating that changes in extreme precipitation are almost uniquely due to the increased humidity of incoming air masses as opposed to changes in the dynamics of storms reaching the Pacific Northwest (e.g., Warner et al. 2015).

It is possible that the mechanisms affecting precipitation extremes on the outer coast is not the same as in King County. In our second study we identified regional clusters of variability across western Oregon and Washington, and found that the Puget Sound lowlands exhibited variability that was distinct from that found on the western slopes of the Olympics and North Cascades. Specifically, we found that 63% of heavy rain events co-occurred in both the Olympics and lower elevations of Puget Sound. For the remaining events, one region experienced high intensity rainfall while the other did not. Our analysis showed that the “Puget Sound” events had more zonal (East-West) flow – which facilitated moisture transport past the Olympics. These events also exhibited a more stable atmosphere – which acted to suppress the rain shadow in the lee of the Olympics.

These results are not sufficient to determine if a statistical model could be used to circumvent the RCM simulations used in the current study. However, they have highlighted a number of avenues for additional exploration. Specifically:

1. Both analyses highlight the importance of the type of storm in diagnosing the drivers of precipitation variability. For example, the mechanisms driving changes in the Common events could be different from those affecting the Puget Sound events identified in the first analysis. Building on the first analysis, one could conduct a more systematic comparison of the historical and future large-scale conditions associated with each type of event. The mechanisms driving changes in each type of storm may be different.
2. There is also important variability within the Puget Sound region – the regional averages in the first analysis could be generalized to smaller sub-regions (e.g., lowland King County) to further distinguish between different types of extreme precipitation events.
3. The results of the second analysis suggest that convective precipitation could be important in determining which areas are affected by extreme precipitation, particularly during the Olympic events. At its current resolution, the WRF model does not adequately capture convective precipitation. Future work could evaluate model performance at different spatial resolutions and test model parameterizations related to precipitation.

Although our results do not provide a definitive conclusion, they do confirm that there are robust relationships between large-scale conditions and local precipitation extremes. Further investigation will be facilitated by new RCM projections and advances in modeling capabilities.

5 Regional Climate Model Simulations

Regional climate model simulations were performed using the Weather Research and Forecasting (WRF, http://www.wrf-model.org; Skamarock et al., 2005) community mesoscale model. WRF is a nonhydrostatic and mesoscale numerical weather model.

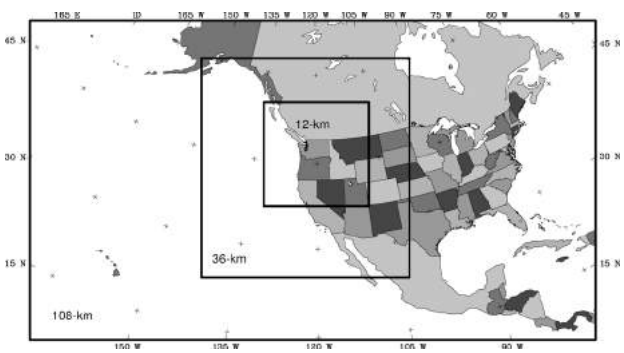

Figure 5.1. Domains for the WRF model: Western US at 36-km and Pacific Northwest at 12-km grid.

Simulations were performed using WRF version 3.2 implemented following Salathé et al. (2010, 2014). Initial and boundary conditions were provided by the two model-scenario pairs identified in Section 2. Lateral boundary conditions and sea surface temperature (SST) were updated once every six hours.

Projections were downscaled to the region using two nested domains (Figure 5.1). The outermost domain at 36-km resolution covers the western North American continent and much of the eastern Pacific Ocean, in order to capture the climatological western flow and the evolution of approaching Atmospheric Rivers (ARs). The innermost domain, at 12-km resolution, encompasses the U.S. Pacific Northwest. One-way nesting was applied in this study.

Thirty vertical levels were used in the model spanning from the surface to 10 hPa, with the finest vertical resolution in the boundary layer. WRF runs were initialized three months prior to the start date of each simulation as spin-up. The physics parameterizations for microphysics, cumulus parameterization, planetary boundary layer, land surface models, and longwave and shortwave radiation are summarized in Lorente et al. (2018). Although we did not perform an extensive validation of the model's performance, previous research has established that it captures the essential characteristics of local-scale weather variations in the Pacific Northwest (e.g., Dulière et al. 2011).

Simulations were performed for the years 1970 through 2099. Results were archived at hourly intervals following Greenwich Mean Time (GMT, which is 8 hours ahead of local standard time in the Pacific Northwest).

6 Observations

Hourly precipitation observations were obtained from three sources: King County, the City of Seattle, and the NOAA Cooperative Observer (COOP) network (Figure 6.1; Tables in Appendix B). All values were converted to millimeters (mm) for the analysis.

Rain gauge observations from King County and the City of Seattle were obtained from King County. The Seattle data are quality controlled by staff at both King County and Seattle. In both cases, the quality control applied to these gauges includes comparison of cumulative distributions, a close evaluation of the highest intensity observations (generally focused on values >0.05 to 0.07" in one minute), and patching data where there are gaps. The data are typically patched using a nearby gauge from either the Seattle or King County networks. The high intensity data is generally only removed if a corresponding high intensity event is not present in other nearby gauges or if there are errors in other fields from recorded by the same gauge (indicating the data may be corrupted).

We obtained the quality controlled Seattle data and aggregated it from minute-by-minute observations to hourly intervals for comparison with the WRF simulations. Following the

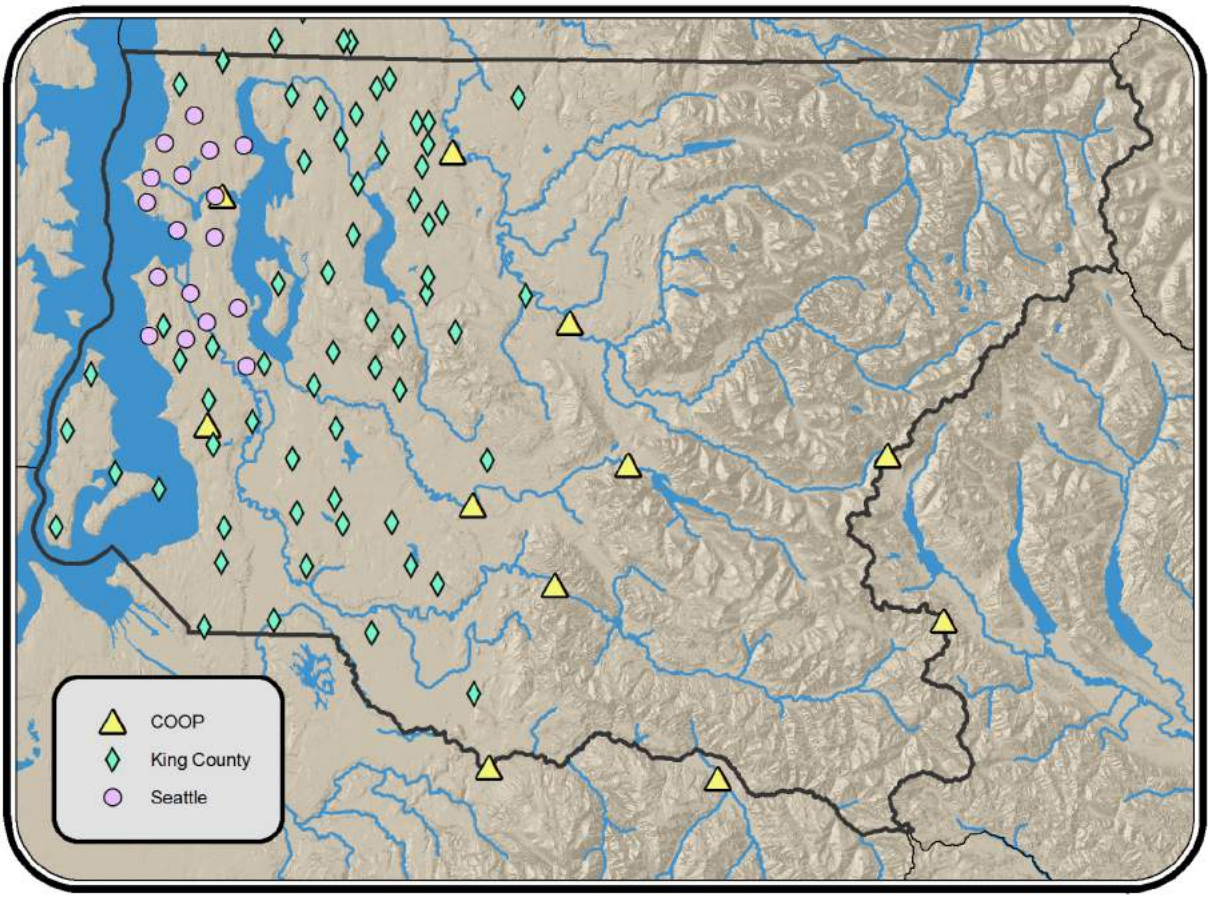

Figure 6.1 Rain gauge locations in King County, with topography shown in the background.

convention, each value in our aggregated record represents the total for the previous hour.

Quality control for the King County gauges followed a similar procedure to that applied to the Seattle gauges (King County 2018). Records are reviewed to identify gaps in the observations, anomalous values, data inconsistencies, or evidence of snow or ice. Comparisons with other stations are used to determine if any anomalous values are consistent with other observations. Quality flags are added to any questionable records. The King County data we obtained had already evaluated these flags and filtered out bad values – no additional quality control was needed.

Additional observations of hourly precipitation were obtained from Cooperative Observer Network (COOP) rain gauge sites through the NOAA National Center for Environmental Information (NCEI; NOAA 2003). COOP stations exist across the region, and many records extend back several decades. We chose to include these in the analysis both as an additional check on the Seattle and King County stations, and as a way of putting local changes in the context of the projections for western Washington as a whole. COOP stations were selected based on the following criteria:

1. Over 30 years from start to end of observational record
2. At least 10% of available data has valid measurements
3. Observations continue through at least 1995

In all, there were 26 COOP stations in western Washington that met these criteria. Data were requested in mm. Although data for all gauges is included in the final results, the gauges highlighted in bold in Table B.3 are most pertinent to the current study.

The COOP data include two quality control flags: a “Measurement” and a “Data Quality” flag. Observations were treated as missing values if any of these flags were present, with one exception: data flagged as Trace precip (“T”) were set to zero (valid data, no precipitation).

Additional inspection of the COOP data revealed periods when precipitation was zero for long stretches, extending beyond one month without precipitation, yet there were no flags to indicate missing data. Data checks with other gauge networks, showed that dry spells of this length do not happen in the region, even in the relatively drier eastern half of the state. As a result, two additional quality control checks were added to the data: (1) data were set to missing when all-zeros stretches extended to more than 60 consecutive days, and (2) COOP stations were only included if 95% of available data was present for at least 30 water years (Oct-Sep). By applying these additional criteria, we were able to remove the vast majority of questionable data.

Finally, two data considerations are worth noting. First, many King County rain gauge records are quite short, limiting the accuracy of the precipitation statistics that can be obtained. This is evident in the results that are presented below. As a result, we recommend a focus on the results for the stations with over 20 years of data. Additional

work is needed to both determine the length of record needed to perform an adequate bias correction and explore options for a regionally generalized bias correction. Second, although we have made every attempt to comprehensively remove errors in the observations, some anomalous values may remain, and these errors could affect the bias correction of the model projections. For this reason, we have included extensive information on model biases, both before and after bias correction, in the products outlined below. In addition, we recommend using the percent changes from the raw projections as opposed to the absolute model projections whenever this is an option.

7 Post-Processing

WRF data extraction

The WRF outputs are on a curvilinear 12-km grid. The model outputs separate precipitation estimates based on whether it is simulated as a result of the convective parameterization occurring at the sub-grid scale or as part of a large-scale process that is resolved by the model. As is typical, precipitation was calculated as the sum of these two quantities.

Hourly data were extracted for the nearest grid point to each rain gauge station (nearest-neighbor interpolation). These constitute the “raw” WRF data for each station dataset. Since the WRF resolution is coarse compared to the spacing of the rain gauge stations, many stations have identical raw WRF data.

Although WRF projections represent a substantial improvement over previous downscaled precipitation estimates, the simulations do contain biases. Many applications require estimates of absolute precipitation totals, especially those that involve continuous simulation of stormwater or other system performance. In these cases, it is not always practical to apply a simple percent change to observed historical precipitation intensities, such as those typically obtained from an intensity-duration-frequency relationship. As a result, the raw WRF data were additionally bias-corrected to match the observations at each rain gauge site.

Bias Correction

For each station location, the raw WRF hourly precipitation was bias corrected to the historical hourly station data. Observed data were quality controlled as described in Section 6, and the full period of record was used for each station.

Although bias correction is a key tool used in many applications, recent work has shown that it can introduce artifacts in the case of climate change, especially when considering changes in extremes (Mauger et al. 2016). In principle one could design a bias correction approach that controls for the sensitivity of climate change. However, such an approach has never been developed and in fact may not be feasible given the limits of observational data and the fact that a statistical approach may not be able to capture complex changes in the processes and responses governing local weather and climate. As a result, our focus in this study is to develop a bias correction approach that strikes a compromise between improved accuracy in the historical simulations while preserving the projected changes from the raw WRF data.

The simplest approach to bias correction is to simply scale the model precipitation so that the model average matches the average in the observations. This is sometimes referred to as the “Delta” method. An advantage of this approach is that it has no effect on the projected changes. However, inspection of the raw model results shows that WRF tends to overestimate the intensity of light rain and underestimate the intensity of heavy rain

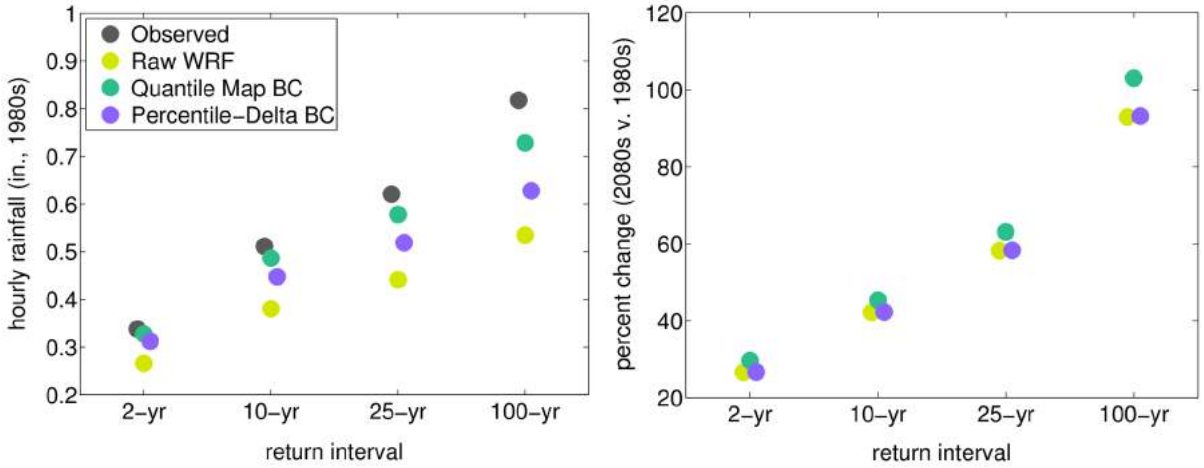

Figure 7.1. Comparison of bias correction approaches for the SeaTac COOP rain gauge station. The figure compares the performance of two bias-correction approaches: the recently-developed quantile mapping approach and the "Percentile-Delta" method used in this study. Both plots show the statistics for the 2-, 10-, 25-, and 100- year extremes in hourly water year precipitation (50%, 10%, 4%, and 1% annual chance of exceedance, respectively). The left-hand plot compares the bias corrected model results to both the raw model results and the observations. Both bias-correction approaches lead to an improvement over the raw results. The right-hand plot compares the percent change in precipitation intensity at each return interval for 2070-2099 (2080s), relative to 1970-1999 (1980s). In this plot we see that the Percentile-Delta approach closely matches the raw projection, while the quantile-mapping approach diverges substantially from the change projected by the model.

events. This suggests that a simple Delta approach will not be adequate, since the bias is not the same for all precipitation intensities. Recent approaches to bias correction have typically emphasized a quantile-mapping approach, in which the probability distribution from the model is adjusted to match the observed probability distribution in precipitation (e.g., Abatzoglou and Brown 2012). While this method is quite effective at reducing the historical biases, including those for the extremes, our tests show that it can introduce substantial biases in the projected changes (Figure 7.1; these results confirm previous findings by Mauger et al. 2016), particularly for extreme events. These discrepancies exist because the correction for one quantile in the historical data can be quite different than the correction for the same quantile in the future due to the projected changes in precipitation intensity and the limited accuracy in estimating the highest quantiles of the distribution. This cannot be readily corrected by removing the long-term trends because the trends are also different for different quantiles. This problem is complicated by the fact that quantile estimates from a finite sample will always have limited accuracy in the extreme tails of the distribution.

For this study, we developed a compromise approach, called the "Percentile-Delta" method, which combines the intensity-based scaling of the quantile mapping approach with the stability of the Delta method. In this approach, the historical and future WRF data are adjusted by correcting mean biases in precipitation in each quantile range (i.e. 0-1, 1-2, … 99-100). First, all model precipitation values below 0.001 inch (0.025 mm) were set to zero. This is a common approach since models simulate a continuous distribution of precipitation yet measurements cannot resolve quantities less than about 0.01 inch (0.25 mm). Next, adjustments were computed in each percentile of precipitation as the

ratio of the average from the historical WRF data (1970-2005) to that from the full observational record. The result is a different set of "deltas" for each percentile. A separate set of percentiles was calculated for the future WRF simulation (2006-2099). These ratios were then applied to all values in each percentile of the historical and future WRF data, respectively. Note that this means that the adjustment applied to a specific precipitation amount (e.g., 5 mm/hr) may be different for the historical and future simulations. This is equivalent to assuming that the mechanisms governing precipitation are a function of the quantile in hourly precipitation as opposed to the total amount. Recent research supports this assumption (e.g., Warner et al. 2015), indicating that a systematic change in storm thermodynamics (increasing water vapor concentration) and not dynamics (e.g., strength or direction of winds) is the primary driver of increases in precipitation intensity.

The Percentile-Delta method was chosen over other methods after extensive testing and evaluation of alternative approaches, applied to both daily and hourly precipitation. The results from these experiments revealed that biases in daily precipitation could be very different than projected changes in hourly precipitation, so that direct bias correction of hourly data was preferable to the bias correction of daily data and subsequent scaling to an hourly time step. In addition, projected changes in return intervals of hourly precipitation were best preserved when performing the Percentile-Delta method versus other methods including quantile-mapping, quantile-mapping with smoothed probability distributions, and applying just two "delta" scalings: one for precipitation below the 99th percentile, and another for all precipitation above it. For all approaches, including the Percentile-Delta method, the degree of historical agreement with observations and consistency with raw model projections differed greatly by station location (e.g., wetter or drier locations) and by the length of the observational record (e.g., shorter records tend to show worse results).

Summary Statistics

Precipitation totals and extreme statistics were calculated for four 30-year time periods: 1970-1999 ("1980s"), 2020-2049 ("2030s"), 2040-2069 ("2050s"), and 2070-2099 ("2080s"). Although longer time periods might be desired to estimate extreme statistics, 30 years was deemed an appropriate compromise between longer periods, which may conflate long-term changes in flood risk with increased sampling of the extremes, and shorter time periods, which can limit the reliability of extremes estimates.

Since limited sample size can lead to errors in either the multi-year averages or extremes statistics, these were only calculated if the following conditions were met:

1. A minimum of 90% valid observations (< 10% missing values) to estimate the maximum or total for the water year or month in question.
2. A minimum of 5 years of valid observations to compute the long-term average (e.g., of total water year precipitation).

3. A minimum 10 years of valid observations to compute the 2-year extreme, and 25 years of valid data to compute the 5-, 10-, 25-, 50-, and 100-year extremes.

These conditions were chosen as a compromise between ensuring that the estimates are robust and the desire to include as many observational records as feasible in the analysis. Caution is advised regarding the results for the 50- and 100-year events, for which a 25-year record will likely be too short to produce robust estimates. For example, in an analysis of precipitation statistics, Lee et al. (2018) estimate a standard deviation of 13% when estimating the 100-year daily precipitation extreme from a 29-year record (estimates of the 2-year event, for comparison, had a standard error of 5%).

Extreme Value Analysis

For many applications, the key metric is the change in the intensity of specific design storms. The raw and bias-corrected data were both processed to estimate exceedance values for both monthly and water year (Oct-Sep) extremes. These calculations followed the standard block-maximum approach, fitted to an extreme distribution using L-moments (Hosking and Wallis 2005).

To calculate extreme statistics, the Extreme Value type 1 distribution described by Gumbel (EV1), the Log-Pearson type 3 (LP3), and the generalized Extreme Value (GEV) distribution with L-moments are commonly used. In this study we apply the GEV distribution with L-moments to estimate extreme precipitation statistics – following the methodology described in Salathé et al. 2014 and Tohver et al. 2014 – based on findings that indicate it is superior to the LP3 distribution (Rahman et al. 1999 & 2015, Vogel et al. 1993, Nick et al. 2011).

Calculations were applied to multiple precipitation durations ranging from 1 hour to 15 days, and the precipitation intensities estimated for following recurrence intervals: 2-, 5-, 10-, 25-, 50-, and 100-year events (50%, 20%, 10%, 4%, 2%, and 1% annual chance of exceedance, respectively).

8 Results

All results from this study are available online and can be accessed via the link below. A Google Map has also been created for identifying stations to facilitate navigation of the results directory. In addition, we have produced a series of summaries and visualizations that can be used to view the results.

- Direct link to results: http://cses.washington.edu/picea/mauger/2017_12_KingCounty_Stormwater/DATA/pub
- Google Map for locating stations: https://goo.gl/6rDsRH
- Interactive visualizations for viewing results: https://doi.org/10.7915/CIG4QJ78R
- Spreadsheet summarizing the projected changes for all durations for the 2030s, 2050s, and 2080s.

The interactive visualizations include three separate viewers to allow users to view model biases relative to observations, view the percent changes for multiple recurrence intervals, and evaluate each of these for different precipitation durations.

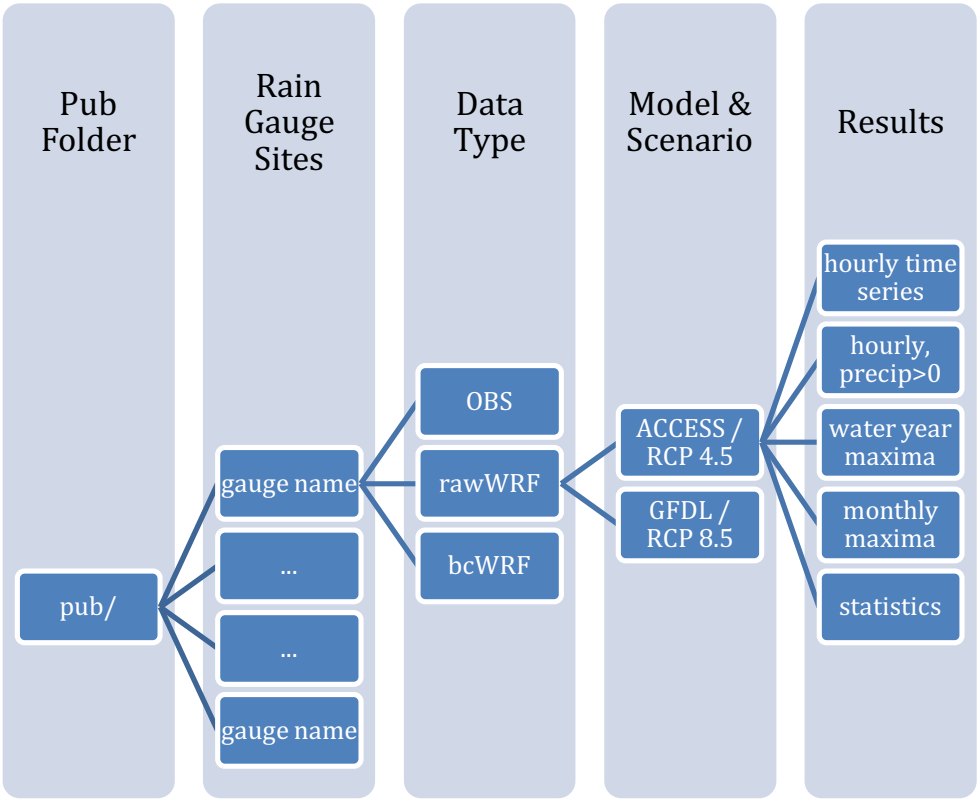

Figure 8.1. Data structure for study results.

Data Structure

The organization of the online repository is shown in Figure 8.1. All files are comma-delimited (.csv), and all values are in millimeters (mm). There are five types of output files, with the following naming conventions:

1. ***Hourly time series files.*** Time series including the full record of observational, raw, and bias-corrected hourly precipitation. For the WRF files these are split into historical (1970-2005) and future (2006-2099) files in order to accommodate the maximum number of rows allowed in Excel. Since the full 130-year hourly time series creates files that are too long for Excel, additional files are provided that separate the historical and future model simulations.

   File naming:

   `<Network>_<ID>_<lat>_<long>_<raw/bcWRF>_<model>_<scenario>.csv`

   `<Network>_<ID>_<lat>_<long>_<raw/bcWRF>_<model>_<scenario>.1970-2005.csv`

   `<Network>_<ID>_<lat>_<long>_<raw/bcWRF>_<model>_<scenario>.2006-2099.csv`

2. ***Time series of non-zero precipitation.*** These are the same as the previous files, except that all zero values of precipitation are removed. For the WRF files, any precipitation value less than 0.001 inch (0.025 mm) were set to zero.

   File naming:

   `<Network>_<ID>_<lat>_<long>_<raw/bcWRF>_<model>_<scenario>.non-zero.csv`

3. ***Water year maxima.*** Maximum precipitation for each water year (Oct-Sep), for 11 different durations (1-, 2-, 3-, 6-, 12-, 24-, 48-, 72-, 120-, 240-, and 360-hour precipitation). These are used as the basis for the extremes calculations described in Section 7.

   File naming:

   `<Network>_<ID>_<lat>_<long>_<raw/bcWRF>_<model>_<scenario>.WYmax.csv`

4. ***Monthly maxima.*** Same as #3 except showing the maximum for each month.

   File naming:

   `<Network>_<ID>_<lat>_<long>_<raw/bcWRF>_<model>_<scenario>.MOmax.csv`

5. ***Extreme Statistics.*** Extreme statistics, for historical and future time periods, for all return intervals and precipitation durations. Two files are included: one listing the absolute totals for each statistic, and another listing the percent change for three future time periods.

   File naming:

   `<Network>_<ID>_<lat>_<long>_<raw/bcWRF>_<model>_<scenario>.stats-abs_vals.csv`

   `<Network>_<ID>_<lat>_<long>_<raw/bcWRF>_<model>_<scenario>.stats-pct_chg.csv`

The observational data file naming is slightly different, since these are not based on a specific model. The file names for these are identical to those listed above, with the following exceptions:

1) The observational data file includes the latitude and longitude of the rain gauge, whereas the WRF files list the position of the nearest model grid point.

2) The WRF-specific suffix '<raw/bcWRF>_<model>_<scenario>' is removed, since it does not apply to the observations.

3) There is no percent change file for the statistics, since future changes are not applicable to the observational record.

Summary: Projected Changes in 1-hour Precipitation Extremes

Projected changes in the 1-hour precipitation statistics are summarized in Table 8.1, for the 2080s (2070-2099) relative to 1970-1999. Projections for other precipitation durations and for the 2030s (2020-2049) and 2050s (2040-2069) are included in the Tableau tool accompanying this report. Each row in the table shows the results for either the total precipitation (1st row), or for different return intervals ranging from the 2- to the 100-year event. Columns show the results for both WRF simulations for the water year, followed by the statistics for each season starting in winter (Dec-Feb) and ending in fall (Sep-Nov).

The percent change in total precipitation is included for comparison with the extreme statistics: models generally show very little change in seasonal and annual totals, whereas studies show more robust changes for the extreme statistics. It is worth noting the significant difference between total precipitation and the extremes statistics. Whereas the total includes all precipitation occurring in a season or water year – including atmospheric rivers, but also smaller storms, drizzle, thunderstorms, etc. In contrast, the extremes are estimated based on only the largest value in each year. This means that changes in total precipitation can be markedly different than projected changes in the extremes.

Focusing on the 25-year event (4% annual chance of exceedance), Table 8.1 shows projected change of -2 to +69% when considering the full water year. Seasonally, the simulations show the largest increase for winter and a tendency for decreases in summer, with more modest increases for spring and fall. Although projected changes differ substantially among return intervals (2-yr event, 5-yr event, etc.), there is some consistency, especially in the projections for summer.

Although global models are more consistent in projecting drier summers, these results are unusual in projecting such large and consistent decreases in summer precipitation. In addition, precipitation extremes in summer can occasionally come in the form of thunderstorms. Whereas atmospheric river events are well captured by both the GCMs and the WRF model, thunderstorms are not well captured by either. Specifically, GCMs are not as adept at representing the large-scale conditions that lead to thunderstorms, in part because these are driven by local variations (e.g., differential surface heating) that

		Water Year		Dec-Feb		Mar-May		Jun-Aug		Sep-Nov	
		ACCESS 1.0 - RCP 4.5 (Low)	GFDL CM3 - RCP 8.5 (High)	ACCESS 1.0 - RCP 4.5 (Low)	GFDL CM3 - RCP 8.5 (High)	ACCESS 1.0 - RCP 4.5 (Low)	GFDL CM3 - RCP 8.5 (High)	ACCESS 1.0 - RCP 4.5 (Low)	GFDL CM3 - RCP 8.5 (High)	ACCESS 1.0 - RCP 4.5 (Low)	GFDL CM3 - RCP 8.5 (High)
Total Precip.		5	4	2	9	-1	16	-38	-38	21	-5
Extreme Statistics	2-yr	21	32	23	17	19	36	-51	-18	14	28
	5-yr	13	45	19	39	24	35	-43	0	14	35
	10-yr	7	54	13	56	28	32	-39	10	17	37
	25-yr	-2	69	2	80	32	26	-34	22	22	37
	50-yr	-9	81	-6	100	36	22	-31	32	27	35
	100-yr	-15	94	-15	122	39	17	-28	41	32	34

Table 8.1. Projected changes (%) in 1-hour precipitation statistics for the WRF grid point closest to the COOP SeaTac rain gauge (#457473), for the 2080s (2070-2099) relative to 1970-1999. Columns show the changes for both WRF scenarios for the full water year (Oct-Sep), as well as for winter (Dec-Feb), spring (Mar-May), summer (Jun-Aug), and fall (Sep-Dec). Rows show the projected change in the total precipitation for each time period as well as the extreme statistics corresponding to the 2-, 5-, 10-, 25-, 50-, and 100-year events.

global models do not resolve. WRF can represent many such variations, but the scale of an individual thunderstorm is still small compared to at 12 km grid cell. At sub-grid scales, such processes are represented statistically in the model and the simulations may not be as accurate. In contrast, atmospheric river events form over thousands of km with little variation in conditions within a 12 km WRF grid cell. It is possible that the projected changes for summer are accurate; further investigation is needed to evaluate the ability of the WRF simulations to accurately capture variations in summer precipitation.

Large differences like this are common across all projections and are a reflection of the intentional choice to bracket the range among projections. However, one confounding effect is the influence of natural variability, which can be particularly important for extreme events. This is illustrated in Figure 8.2, which simply shows the time series of the annual maximum for 1- and 24-hour precipitation for each water year. Consistent with Table 8.1, these show a clear tendency towards larger events in the GFDL simulation. In contrast, no clear trend is evident in the ACCESS simulation, suggesting that the changes estimated from this simulation reflect random natural variability as opposed to a long-term trend.

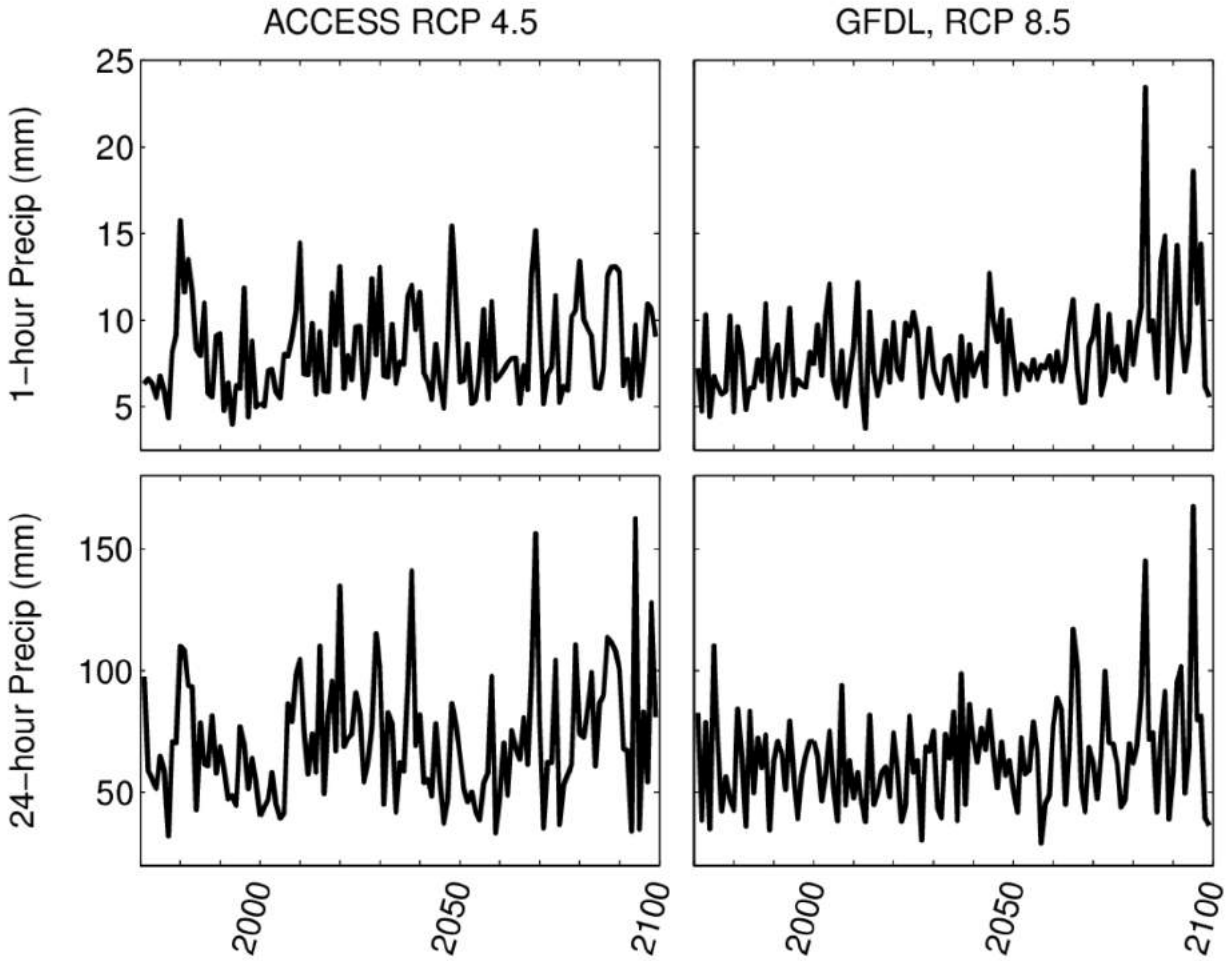

Figure 8.2. Time series of the water year maximum in 1-hour (top row) and 24-hour (bottom row) precipitation for the Sea-Tac NOAA weather station site (ID: 457473. Results are shown for the ACCESS-RCP4.5 (left) and GFDL-RCP8.5 (right) simulations.

A number of considerations have been discussed throughout the text that may be helpful to keep in mind when reviewing the projections. For convenience, these are summarized below:

- Projected changes will always be governed by a combination of random variability and long-term trends due to climate change. This is particularly true for changes in extremes: Since by definition these events are rare, it is difficult to accurately assess how rapidly they will change. Although even the 2080s projections can be significantly influenced by natural variability, we recommend focusing on these late century projections since this is when the projected changes will be largest relative to natural variability.

- The extremes estimates are limited by sample size. Whereas the 2- and 5-year events are relatively well captured in a 30-year record (e.g., 1970-1999, 2070-2099), extrapolation is needed to estimate the 50- and 100-year extremes. This means that the 50- and 100-year estimates are more prone to noise. For example,

if the simulation includes one particularly large storm in the historical record, this could artificially mute the projected change estimates even if, on average, most storms do become more intense. The converse is also true: a large storm at the end of the 21st century could artificially inflate the estimated change.

- Projected changes differ substantially for different precipitation durations. In general, changes appear to be largest for 1-hour precipitation and smallest for the longest durations. This is consistent with previous research projecting a change in atmospheric river events yet very little change in seasonal precipitation.

- As Table 8.1 suggests, the models do tend to correspond to their "Low" and "High" titles for the winter and water year statistics. Since the largest atmospheric rivers tend to occur in winter, this is appropriate. In other seasons, the GFDL projection tends to be higher, but the results are more mixed. As Figures 3.3 and 3.4 suggest, the two bracketing models will not correspond to the extremes among all GCMs and scenarios for all metrics and all times.

- Similarly, the two projections are unlikely to bracket the full range of potential future outcomes. Instead, these should be viewed as two equally-likely futures which should be accounted for in planning and design. Future work can provide additional WRF simulations, from which we could obtain a more robust estimate of the mean and range among projections.

- The WRF model used in this study has a spatial resolution of 12 km. This is not enough to explicitly resolve convective precipitation, such as thunderstorms. Although these are represented statistically by the model, researchers generally consider that a finer resolution is needed to accurately capture convective events. This means that the current projections should be viewed primarily as an estimate of the change in the intensity of large-scale heavy precipitation events such as atmospheric rivers. Since thunderstorms are most prevalent in summer, this limitation in the WRF model is most likely to affect projected changes in summer precipitation events.

- In this study, extremes were estimated by fitting a GEV distribution with L-moments (Section 6). This approach will result in different estimates than the standard (e.g., Bulletin 17B, 1982) methods that are prescribed in certain applications. In most cases, these differences should be minor. However, we recommend repeating the calculations using the prescribed methodology to ensure consistent results and interpretation.

Discussion

There are two primary achievements in the current study:

1. Successful application of dynamical downscaling to the new set of global climate model projections, and

2. Development of an approach to tailoring the new results for use in stormwater planning.

This entailed a number of efforts, ranging from model evaluation and selection, refinement of bias correction approaches, and the development of specific products that can be used in settings ranging from rural stormwater to urban wastewater.

As intended, the two projections offer different perspectives on the future risks due to changing heavy precipitation. Selected to bracket the range among all models, the high-end projection (GFDL-RCP8.5) indicates the potential for large increases in storm intensity, which would have significant impacts on stormwater, wastewater, and river management. In contrast, the low-end projection (ACCESS-RCP4.5) generally indicates more modest increases, and even some decreases, in precipitation intensity. Further inspection revealed that the changes observed in the low-end projection are primarily a consequence of natural variability as opposed to a long-term trend. This suggests that the ACCESS-RCP4.5 projection is best viewed as a “no change” scenario (with respect to rain intensity), and that any apparent changes in precipitation are likely a consequence of random natural variability.

There are two primary factors that make it difficult to interpret these results:

1. It is difficult to detect changes in the frequency of rare events, and
2. With only two global model projections, it is not possible to estimate the distribution of projections

Both of these issues can be addressed by obtaining additional regional climate model projections. These can be obtained via a collaboration with UW Professor Cliff Mass, who is currently producing several new regional model projections under a grant from the Amazon Catalyst program. These new projections would help elucidate our results in two ways: by both increasing the sample size, thereby improving the statistics; and by evaluating results for new global models, which may have different model representations for key processes.

In addition to the two issues outlined above, we believe there are a number of methodological choices that could be investigated further. There are two issues in particular that merit further study: (1) regionalized precipitation statistics, and (2) optimizing the WRF model configuration. For the first, extreme precipitation statistics can be “regionalized” by assuming that extremes across the county follow a similar distribution. This improves the reliability of extremes estimates, particularly for gauges with short records. This information could also be used to further improve the bias correction approach. The second effort could be scaled depending on the time and resources that are available; the focus would be to compare the performance of the WRF model for different spatial resolutions and parameterizations affecting precipitation formation. For example, the current resolution of 12 km does not appear adequate for capturing convective precipitation events, such as thunderstorms.

Finally, the domain of the WRF model used to develop these projections covers the entire Pacific Northwest, stretching from northern California to British Columbia and from the west coast through the Rocky Mountains of Montana and Wyoming. This means that the results of these new projections can be evaluated for other communities around the region. This work has already begun: the City of Everett, the Port Gamble S'Klallam Tribe, and Thurston County have all leveraged King County's investment to evaluate changes in precipitation extremes for their jurisdictions at a much lower additional cost. As interest in this work grows, additional coordination may be warranted to capitalize on similar economies of scale.

References

Abatzoglou, J. T., & Brown, T. J. (2012). A comparison of statistical downscaling methods suited for wildfire applications. International Journal of Climatology, 32(5), 772-780. http://onlinelibrary.wiley.com/doi/10.1002/joc.2312/full

Bi D, Dix M, Marsland S, O'Farrell S, Rashid H, Uotila P, et al. The Access Coupled Model: Description, Control Climate and Evaluation. Australian Meteorological and Oceanographic Journal. 2013; 63:41-64. http://dx.doi.org/10.22499/2.6301.004

Brekke, L. D., Dettinger, M. D., Maurer, E. P., & Anderson, M. (2008). Significance of model credibility in estimating climate projection distributions for regional hydroclimatological risk assessments. *Climatic Change*, *89*(3-4), 371-394. http://dx.doi.org/10.1007/s10584-007-9388-3

(Bulletin 17-B) U.S. Interagency Advisory Committee on Water Data, 1982, Guidelines for determining flood flow frequency, Bulletin 17-B of the Hydrology Subcommittee: Reston, Virginia, U.S. Geological Survey, Office of Water Data Coordination, [183 p.]. [Available from National Technical Information Service, Springfield VA 22161 as report no. PB 86 157 278 or from FEMA at http://www.fema.gov/mit/tsd/dl_flow.htm

Dulière, V., Zhang, Y., & Salathé Jr, E. P. (2011). Extreme precipitation and temperature over the US Pacific Northwest: A comparison between observations, reanalysis data, and regional models. Journal of Climate, 24(7), 1950-1964.

Griffies, S. M., Winton, M., Donner, L. J., Horowitz, L. W., Downes, S. M., Farneti, R., ... & Palter, J. B. (2011). The GFDL CM3 coupled climate model: characteristics of the ocean and sea ice simulations. *Journal of Climate*, *24*(13), 3520-3544. https://doi.org/10.1175/2011JCLI3964.1

Hosking, J. R. M., & Wallis, J. R. (2005). Regional frequency analysis: an approach based on L-moments. Cambridge University Press.

IPCC, 2013: Summary for Policymakers. In: Climate Change 2013: The Physical Science Basis. Contribution of Working Group I to the Fifth Assessment Report of the Intergovernmental Panel on Climate Change [Stocker, T.F., D. Qin, G.-K. Plattner, M. Tignor, S.K. Allen, J. Boschung, A. Nauels, Y. Xia, V. Bex and P.M. Midgley (eds.)]. Cambridge University Press, Cambridge, United Kingdom and New York, NY, USA

IPCC, 2014: Summary for Policymakers. In: Climate Change 2014: Mitigation of Climate Change. Contribution of Working Group III to the Fifth Assessment Report of the Intergovernmental Panel on Climate Change [Edenhofer, O., R. Pichs-Madruga, Y. Sokona, E. Farahani, S. Kadner, K. Seyboth, A. Adler, I. Baum, S. Brunner, P. Eickemeier, B. Kriemann, J. Savolainen, S. Schlömer, C. von Stechow, T. Zwickel

and J.C. Minx (eds.)]. Cambridge University Press, Cambridge, United Kingdom and New York, NY, USA.

Kalnay, E., Kanamitsu, M., Kistler, R., Collins, W., Deaven, D., Gandin, L., ... & Zhu, Y. (1996). The NCEP/NCAR 40-year reanalysis project. Bulletin of the American meteorological Society, 77(3), 437-471.

King County (2018). *King County Standard Operating Procedures for Collection of Rainfall Data.* Department of Natural Resources and Parks, King County.

Kaufmann, P., & Weber, R. O. (1996). Classification of mesoscale wind fields in the MISTRAL field experiment. Journal of Applied Meteorology, 35(11), 1963-1979.

Lee, S.-Y., G. Mauger, and J. Won. 2018. Effect of Climate Change on flooding in King County Rivers. Report prepared for King County. Climate Impacts Group, University of Washington.

Lorente-Plazas, R., T. P. Mitchell, G. S. Mauger, E. P. Salathé Jr. (2018). Atmospheric rivers induce local extreme precipitation in the U.S. Pacific Northwest through interactions with the orography. *J. Hydrometeorology. In Review.*

Lynch, C.D. and G.S. Mauger. Consider the source: Ranking global models by evaluating the large-scale drivers of precipitation. *Manuscript in preparation.*

Mass, C. (1981). Topographically forced convergence in western Washington State. Monthly Weather Review, 109(6), 1335-1347.

Mauger, G.S., S.-Y. Lee, C. Bandaragoda, Y. Serra, J.S. Won, (2016). Refined Estimates of Climate Change Affected Hydrology in the Chehalis basin. Report prepared for Anchor QEA, LLC. Climate Impacts Group, University of Washington, Seattle. https://doi.org/10.7915/CIG53F4MH

Mauger, G.S., J.H. Casola, H.A. Morgan, R.L. Strauch, B. Jones, B. Curry, T.M. Busch Isaksen, L. Whitely Binder, M.B. Krosby, and A.K. Snover, 2015. State of Knowledge: Climate Change in Puget Sound. Report prepared for the Puget Sound Partnership and the National Oceanic and Atmospheric Administration. Climate Impacts Group, University of Washington, Seattle. https://doi.org/10.7915/CIG93777D

Meehl, G. A., C. Covey, T. Delworth, M. Latif, B. McAvaney, J. F. B. Mitchell, R. J. Stouffer, and K. E. Taylor, 2007: The WCRP CMIP3 multi-model dataset: A new era in climate change

Nick, M., Das, S. and Simonovic, S.P. 2011. The Comparison of GEV, Log-Pearson Type 3 and Gumbel Distributions in the Upper Thames River Watershed under Global Climate Models, the University of Western Ontario Department of Civil and Environmental Engineering, Report No:077. https://ir.lib.uwo.ca/wrrr/40/

North, G. R., Bell, T. L., Cahalan, R. F., & Moeng, F. J. (1982). Sampling errors in the estimation of empirical orthogonal functions. Monthly Weather Review, 110(7), 699-706.

(NOAA) U.S. Department of Commerce, National Oceanic and Atmospheric Administration, National Centers for Environmental Information (NCEI). (2003). *DATA DOCUMENTATION FOR DATA SET 3240 (DSI-3240); Hourly Precipitation Data*. https://www.ncdc.noaa.gov/IPS/hpd/hpd.html

Rahman, A., Weinmann, P.E. and Mein, R.G. (1999). At-site flood frequency analysis: LP3-product moment, GEV-L moment and GEV-LH moment procedures compared. In: Proceeding Hydrology and Water Resource Symposium, Brisbane, 6–8 July, 2, 715–720.

Rahman, A., Karin, F, and Rahman, A. 2015. Sampling Variability in Flood Frequency Analysis: How Important is it? 21st International Congress on Modelling and Simulation, Gold Coast, Australia, Nov 29-Dec 4, 2015, 2200-2206.

Roeckner, E., Bäuml, G., Bonaventura, L., Brokopf, R., Esch, M., Giorgetta, M., et al. (2003). The atmospheric general circulation model ECHAM 5. PART I: Model description.Report / MPI für Meteorologie, 349.

Rosenberg, E. A., Keys, P. W., Booth, D. B., Hartley, D., Burkey, J., Steinemann, A. C., & Lettenmaier, D. P. (2010). Precipitation extremes and the impacts of climate change on stormwater infrastructure in Washington State. Climatic Change, 102(1-2), 319-349.

Ryoo, J. M., Y. Kaspi, D. W. Waugh, G. N. Kiladis, D. E. Waliser, E. J. Fetzer, and J. Kim, (2013). Impact of Rossby Wave Breaking on U.S. West Coast Winter Precipitation during ENSO Events. *J. Climate*, 26, 6360-6382.

Salathé Jr., Eric P., Alan F. Hamlet, Clifford F. Mass, Se-Yeun Lee, Matt Stumbaugh, and Richard Steed, 2014: Estimates of Twenty-First-Century Flood Risk in the Pacific Northwest Based on Regional Climate Model Simulations. J. Hydrometeor, 15, 1881–1899. doi: http://dx.doi.org/10.1175/JHM-D-13-0137.1

Scheff, J., & Frierson, D. M. (2012). Robust future precipitation declines in CMIP5 largely reflect the poleward expansion of model subtropical dry zones. Geophysical Research Letters, 39(18).

Siler, N., & Durran, D. (2016). What causes weak orographic rain shadows? Insights from case studies in the Cascades and idealized simulations. Journal of the Atmospheric Sciences, 73(10), 4077-4099.

Sillmann, J., V. V. Kharin, F. W. Zwiers, X. Zhang, and D. Bronaugh, 2013a: Climate extremes indices in the CMIP5 multimodel ensemble: Part 2. Future climate projections. *Journal of Geophysical Research Atmos.*, **118**: 2473–2493, http://dx.doi.org/10.1002/jgrd.50188

Sillmann, J., V. Kharin, X. Zhang, F. Zwiers, and D. Bronaugh, 2013b: Climate extremes indices in the CMIP5 multimodel ensemble: Part 1. Model evaluation in the present climate. *Journal of Geophysical Research: Atmospheres*, **118**(4): 1716-1733. http://dx.doi.org/10.1002/jgrd.50203

Skamarock, W. C., Klemp, J. B., Dudhia, J., Gill, D. O., Barker, D. M., Wang, W., & Powers, J. G. (2005). *A description of the advanced research WRF version 2* (No. NCAR/TN-468+ STR). National Center For Atmospheric Research Boulder Co Mesoscale and Microscale Meteorology Div.

Tohver, I. M., Hamlet, A. F., & Lee, S. Y. (2014). Impacts of 21st-Century Climate Change on Hydrologic Extremes in the Pacific Northwest Region of North America. JAWRA Journal of the American Water Resources Association, 50(6), 1461-1476. https://doi.org/10.1111/jawr.12199

Trenberth, K. E. (2011). Changes in precipitation with climate change. Climate Research, 47(1-2), 123-138. http://dx.doi.org/10.3354/cr00953

Van Vuuren, D., J. Edmonds, M. Kainuma, K. Riahi, A. Thomson, K. Hibbard, G. Hurtt, T. Kram, V. Krey, J. Lamarque, T. Masui, M. Meinshausen, N. Nakicenovic, S. Smith, S. Rose, 2011: The representative concentration pathways: an overview. *Climatic Change*, **109**: 5-31. http://dx.doi.org/10.1007/s10584-011-0148-z

Vogel, R.M., McMahon, T.A. and Chiew, F.H.S. (1993). Flood flow frequency model selection in Australia, Journal Hydrology, 146, 421-449. https://doi.org/10.1016/0022-1694(93)90288-K

Ward Jr, J. H. (1963). Hierarchical grouping to optimize an objective function. Journal of the American statistical association, 58(301), 236-244.

Warner, M. D., Mass, C. F., & Salathé Jr, E. P. (2015). Changes in winter atmospheric rivers along the North American west coast in CMIP5 climate models. *Journal of Hydrometeorology*, *16*(1), 118-128. https://doi.org/10.1175/JHM-D-14-0080.1

Wilks, D. (1995). Statistical Methods in Atmospheric Sciences: An Introduction. Academic Press.

Appendix A: Global Climate Models (GCMs)

Table A.1. Global Climate Models that were evaluated and ranked for this study. Note that many institutions include several versions of their model in the Coupled Model Intercomparison Project (CMIP) archive. All models are relatively coarse in spatial resolution, but the spacing varies substantially among models. Climate scenarios are discussed in detail in Section 3 and Mauger et al. (2015).

Model	*Source*	*Resolution (deg.)*	*Vertical Levels*
ACCESS1-0	Commonwealth Scientific and Industrial Research Organization, Australia/ Bureau of Meteorology, Australia	1.25 × 1.88	38
bcc-csm1-1	Beijing Climate Center, China Meteorological Administration	2.8 × 2.8	26
bcc-csm1-1-m	Beijing Climate Center, China Meteorological Administration	1.12 × 1.12	26
BNU-ESM	College of Global Change and Earth System Science, Beijing Normal University, China	2.8 × 2.8	26
CanESM2	Canadian Centre for Climate Modeling and Analysis	2.8 × 2.8	35
CCSM4	National Center of Atmospheric Research, USA	1.25 × 0.94	26
CESM1-BGC	Community Earth System Model Contributors	1.25 × 0.94	26
CESM1-CAM5	Community Earth System Model Contributors	1.25 × 0.94	26
CESM1-FASTCHEM	Community Earth System Model Contributors	1.25 × 0.94	26
CESM1-WACCM	Community Earth System Model Contributors	2.5 × 1.89	66
CNRM-CM5	National Centre of Meteorological Research, France	1.4 × 1.4	31
CSIRO-Mk3-6-0	Commonwealth Scientific and Industrial Research Organization/ Queensland Climate Change Centre of Excellence, Australia	1.8 × 1.8	18
EC-EARTH	EC-EARTH consortium	1.13 × 1.12	62
FGOALS-g2	LASG, Institute of Atmospheric Physics, Chinese Academy of Sciences	2.8 × 2.8	26
GFDL-CM3	NOAA Geophysical Fluid Dynamics Laboratory, USA	2.5 × 2.0	48
GFDL-ESM2G	NOAA Geophysical Fluid Dynamics Laboratory, USA	2.5 × 2.0	48
GISS-E2-H	NASA Goddard Institute for Space Studies, USA	2.5 × 2.0	40
GISS-E2-R	NASA Goddard Institute for Space Studies, USA	2.5 × 2.0	40
HadCM3	Met Office Hadley Center, UK	3.75 × 2.5	19
HadGEM2-AO	Met Office Hadley Center, UK	1.88 × 1.25	38

Model	*Source*	*Resolution (deg.)*	*Vertical Levels*
HadGEM2-CC	Met Office Hadley Center, UK	1.88 × 1.25	60
HadGEM2-ES	Met Office Hadley Center, UK	1.88 × 1.25	38
inmcm4	Institute for Numerical Mathematics, Russia	2.0 × 1.5	21
IPSL-CM5A-LR	Institut Pierre Simon Laplace, France	3.75 × 1.8	39
IPSL-CM5A-MR	Institut Pierre Simon Laplace, France	2.5 × 1.25	39
MIROC5	Atmosphere and Ocean Research Institute (The University of Tokyo), National Institute for Environmental Studies, and Japan Agency for Marine-Earth Science and Technology	1.4 × 1.4	40
MIROC-ESM	Japan Agency for Marine-Earth Science and Technology, Atmosphere and Ocean Research Institute (The University of Tokyo), and National Institute for Environmental Studies.	2.8 × 2.8	80
MPI-ESM-LR	Max Planck Institute for Meteorology, Germany	1.88 × 1.87	47
MPI-ESM-MR	Max Planck Institute for Meteorology, Germany	1.88 × 1.87	95
MRI-CGCM3	Meteorological Research Institute, Japan	1.1 × 1.1	48
MRI-ESM1	Meteorological Research Institute, Japan	1.1 × 1.1	50
NorESM1-M	Norwegian Climate Center, Norway	2.5 × 1.9	26

Appendix B: Rain Gauges

Table B.1. King County Rain Gauges used in this study. Gauges are listed in order from the longest to shortest observational record.

Station Name	*ID*	*Location*	*Dates*	*Yrs*
East Fork Issaquah	14u	47.53170N / 121.98718W	09/30/1987--04/28/2016	28
Hollywood Hill	51w	47.72625N / 122.12411W	09/30/1987--04/28/2016	28
McDonald Creek	25v	47.47884N / 122.05988W	09/30/1987--04/18/2016	28
Norway	51u	47.74167N / 122.20983W	09/30/1987--04/28/2016	28
Tibbetts Creek	67u	47.52670N / 122.06297W	09/30/1987--04/28/2016	28
Juanita Creek	27u	47.73061N / 122.17117W	09/30/1988--04/28/2016	27
Lake Dolloff	41v	47.32145N / 122.29200W	09/30/1988--04/28/2016	27
Lower Green River	32u	47.31956N / 122.17971W	09/30/1988--04/28/2016	27
Panther Creek	03u	47.41557N / 122.20032W	09/30/1988--04/28/2016	27
Star Lake	41u	47.35259N / 122.28914W	09/30/1988--04/28/2016	27
Boeing Creek	04u	47.74965N / 122.35963W	09/30/1989--04/28/2016	26
Lake Reba	42u	47.46666N / 122.31327W	08/01/1990--04/28/2016	25
Lower May Creek	37u	47.51235N / 122.14882W	09/30/1990--04/28/2016	25
Brugger's Bog	35u	47.77198N / 122.30305W	09/30/1991--04/28/2016	24
Des Moines Creek	11u	47.42708N / 122.30621W	09/30/1991--04/28/2016	24
Jenkins Creek	26u	47.35956N / 122.06755W	07/23/1991--04/28/2016	24
Middle Green	40u	47.26070N / 122.09187W	07/23/1991--04/18/2016	24
Salmon Creek	50u	47.50197N / 122.35185W	09/30/1991--04/28/2016	24
Soos Creek	54v	47.37961N / 122.14360W	09/30/1991--04/28/2016	24
Blakely Ridge	02v	47.71857N / 122.04295W	09/30/1989--03/19/2013	23
Cottage Lake	02w	47.75758N / 122.08026W	09/30/1992--04/28/2016	23
Hobart	31z	47.41681N / 121.94282W	09/30/1994--04/28/2016	21
Cougar Mountain	63y	47.54110N / 122.09838W	09/30/1996--04/27/2016	19
East Fork Hylebos	24v	47.26284N / 122.31267W	07/19/1996--04/28/2016	19
Hamm Creek	hau	47.51488N / 122.30945W	09/30/1995--12/02/2014	19
Enumclaw	44u	47.20740N / 121.95570W	02/12/1998--04/28/2016	18
North Vashon	43u	47.48771N / 122.46985W	09/30/1998--04/28/2016	17
Bellevue Crossroads I&I	XRDS	47.61734N / 122.12562W	09/30/2000--04/28/2016	15
Black Diamond I&I	BDIA	47.30523N / 122.00601W	09/30/2000--04/28/2016	15
Kent-Kangley I&I	KANG	47.35785N / 122.13277W	09/30/2000--04/28/2016	15
Kirkland I&I	KIRK	47.68230N / 122.19228W	09/30/2000--04/28/2016	15
Lake Serene I&I	SERE	47.87185N / 122.29195W	09/30/2000--04/28/2016	15
Lakeland Hills - Orovitz Pump Station I&I	LHPS	47.26995N / 122.22085W	09/30/2000--04/28/2016	15

Station Name	*ID*	*Location*	*Dates*	*Yrs*
Little Bear I&I	BEAR	47.79037N / 122.13289W	09/30/2000--04/28/2016	15
Mercer Island I&I	MERC	47.57218N / 122.22380W	09/30/2000--04/28/2016	15
Mystic Lake	18Y	47.62790N / 122.02493W	09/30/2000--04/28/2016	15
North Creek Maltby I&I	MNCR	47.81789N / 122.19762W	09/30/2000--01/08/2016	15
Novelty Hill I&I	NOVH	47.69184N / 122.08887W	09/30/2000--04/28/2016	15
Renton Roads	31UN	47.48189N / 122.17426W	12/06/2000--04/28/2016	15
Sahale I&I	SAHA	47.64949N / 122.04403W	09/30/2000--04/28/2016	15
Sammamish Plateau I&I	SAMP	47.58047N / 122.02526W	09/30/2000--02/03/2016	15
Sequoia JR High School I&I	SEQU	47.36701N / 122.19304W	09/30/2000--04/28/2016	15
Tukwilla I&I	TUKW	47.44845N / 122.25478W	09/30/2000--04/28/2016	15
Upper May Creek	37W	47.49867N / 122.09275W	09/30/2000--01/14/2016	15
Bothell I&I	BOTH	47.79104N / 122.23285W	09/30/2001--01/08/2016	14
Factoria I&I	FACT	47.58314N / 122.15806W	09/30/2001--04/28/2016	14
Martha Lake I&I	MCSN	47.85867N / 122.23930W	09/30/2001--01/11/2016	14
Marymoor Park I&I	MARY	47.66354N / 122.12015W	09/30/2001--04/28/2016	14
Patterson Creek Upper @ Nursery	48Y	47.63892N / 122.00776W	03/14/2002--04/28/2016	14
Covington Creek	09V	47.32160N / 122.04125W	09/30/2004--04/18/2016	11
East Maury Island	36V	47.38630N / 122.37609W	03/25/2005--04/28/2016	11
Maury Island	36U	47.39959N / 122.43448W	10/05/2004--04/28/2016	11
Tahlequah	65U	47.35050N / 122.51111W	11/05/2004--04/28/2016	11
West Judd Creek	28Y	47.43699N / 122.49933W	10/05/2004--04/28/2016	11
Brightwater	BW-rain	47.79171N / 122.14292W	09/30/2005--04/27/2016	10
Lakeridge Elementary School	SKY1	47.50039N / 122.24068W	03/12/2003--11/27/2013	10
Sammamish River	51T	47.70302N / 122.14366W	09/18/2005--04/28/2016	10
Trilogy Golf Course	Trilogy-met	47.69998N / 122.02790W	05/31/2005--04/15/2016	10
Cherry Creek	05u	47.74258N / 121.90845W	09/10/2008--03/30/2016	7
Boulder Cr Apts	BC-Rain	47.56589N / 122.02631W	10/21/2009--04/28/2016	6
Fairwood	31Y2	47.44325N / 122.14350W	09/30/2009--04/28/2016	6
Redmond Ridge	18V2	47.67940N / 122.03476W	02/26/2010--04/28/2016	6
Twin Cedars	19U	47.56529N / 121.89455W	10/12/2009--04/28/2016	6
Barton	BART	47.53276N / 122.37478W	04/22/2011--04/28/2016	5
Cold Creek	CL-MET	47.74987N / 122.09711W	05/12/2006--01/22/2010	3
Trilogy North	02VN	47.71939N / 122.02765W	09/30/2013--04/28/2016	2

Table B.2. Seattle Rain Gauges used in this study. Since all records have the same length, stations are listed in order based on the gauge ID.

Station Name	*ID*	*Location*	*Dates*	*Yrs*
N 128th St	rg01	47.72188N / 122.33946W	01/01/1976--03/01/2016	40
NE 93rd St	rg02	47.69629N / 122.27314W	01/01/1976--03/01/2016	40
NE Pacific St	rg03	47.64962N / 122.30881W	01/01/1976--03/01/2016	40
NE 86th St	rg04	47.69077N / 122.31815W	01/01/1976--03/01/2016	40
Fauntleroy Ferry Doc	rg05	47.52331N / 122.39397W	01/01/1976--03/01/2016	40
15th Ave NW	rg07	47.69712N / 122.37819W	01/01/1976--03/01/2016	40
Gov't locks	rg08	47.66544N / 122.39590W	01/01/1976--03/01/2016	40
Woodland Park Zoo	rg09	47.66830N / 122.35385W	01/01/1976--03/01/2016	40
Beacon Ave S	rg10	47.49830N / 122.26344W	01/01/1976--03/01/2016	40
Denny St	rg11	47.61861N / 122.35975W	01/01/1976--03/01/2016	40
34th Ave W	rg12	47.64309N / 122.40042W	01/01/1976--03/01/2016	40
Walnut Ave W	rg14	47.57603N / 122.38419W	01/01/1976--03/01/2016	40
Diagonal Ave S	rg15	47.56231N / 122.33996W	01/01/1976--03/01/2016	40
East Marginal Wy S	rg16	47.53666N / 122.31812W	01/01/1976--03/01/2016	40
SW Barton St	rg17	47.52092N / 122.34518W	01/01/1976--03/01/2016	40
Ranier Ave S	rg18	47.54961N / 122.27714W	01/01/1976--03/01/2016	40
E Union St	rg20	47.61307N / 122.30955W	01/01/1976--03/01/2016	40

Table B.3. NOAA Cooperative (COOP) Network Rain Gauges used in this study. As in Table B.1, gauges are listed in order from longest to shortest observational record. Stations that are within or near King County are highlighted in bold.

Station Name	*ID*	*Location*	*Dates*	*Yrs*
BURLINGTON	450986	48.46720N / 122.31360W	07/04/1948--01/01/2014	65
CLEARWATER	451496	47.57110N / 124.29220W	07/01/1948--01/01/2014	65
COUGAR 4 SW	451759	46.00860N / 122.34550W	07/01/1948--01/01/2014	65
CUSHMAN DAM	451934	47.42380N / 123.21970W	07/19/1948--01/01/2014	65
EVERETT	**452675**	**47.97520N / 122.19500W**	**07/04/1948--01/01/2014**	**65**
MARBLEMOUNT RANGER STATION	454999	48.53800N / 121.45020W	07/06/1948--01/01/2014	65
QUILCENE 5 SW DAM	456851	47.78470N / 122.97970W	09/26/1948--01/01/2014	65
SNOQUALMIE PASS	**457781**	**47.42470N / 121.41380W**	**07/01/1948--09/01/2013**	**65**
SPOKANE INTERNATIONAL AIRPORT	457938	47.62160N / 117.52800W	08/01/1948--12/30/2013	65
STAMPEDE PASS	**458009**	**47.27670N / 121.33720W**	**07/01/1948--12/31/2013**	**65**
PALMER 3 ESE	**456295**	**47.30580N / 121.85130W**	**07/01/1948--02/01/2013**	**64**
MUD MOUNTAIN DAM	**455704**	**47.14130N / 121.93550W**	**07/04/1948--02/01/2010**	**61**
PORT ANGELES	456624	48.11380N / 123.43160W	07/01/1948--11/01/2008	60
MONTESANO 1 S	455549	46.96750N / 123.60640W	08/01/1954--01/01/2014	59
OLYMPIA AIRPORT	456114	46.97330N / 122.90330W	08/15/1954--12/31/2013	59
SNOQUALMIE FALLS	**457773**	**47.54130N / 121.83610W**	**08/01/1954--09/01/2013**	**59**
LANDSBURG	454486	47.37660N / 121.96130W	08/01/1954--02/01/2013	58
ABERDEEN 20 NNE	450013	47.26130N / 123.71470W	07/01/1948--11/02/2004	56
CEDAR LAKE	**451233**	**47.41440N / 121.75610W**	**08/01/1953--01/01/2010**	**56**
CARNATION 4 NW	**451146**	**47.69306N / 121.99472W**	**07/04/1948--02/01/2003**	**54**
WESTPORT 2 S	459112	46.87083N / 124.10833W	08/05/1948--03/01/2003	54
GREENWATER	**453357**	**47.13333N / 121.63333W**	**07/04/1948--01/01/1999**	**50**
SAPPHO 8 E	457319	48.06667N / 124.11667W	07/04/1948--04/01/1998	49
SEATTLE TACOMA INTERNATIONAL AIRPORT	**457473**	**47.44440N / 122.31380W**	**01/01/1965--12/31/2013**	**49**
QUILLAYUTE STATE AIRPORT	456858	47.93750N / 124.55500W	08/01/1966--12/31/2013	47
GRAYS RIVER	453329	46.36667N / 123.56667W	08/01/1954--05/01/1991	36
SEATTLE PORTAGE BAY	**457458**	**47.65000N / 122.30000W**	**03/01/1973--07/01/1998**	**25**

“Urban Stormwater”, by Victoria Pinheiro